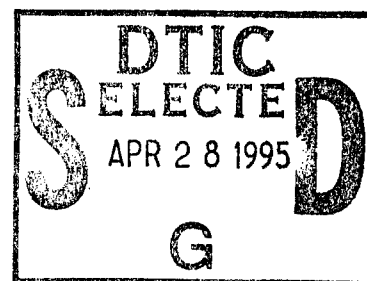


# NAVAL POSTGRADUATE SCHOOL MONTEREY, CALIFORNIA



## THESIS

### EFFECTS OF MOSAICITY ON PARAMETRIC X-RADIATION PRODUCTION

by

William Morgan Buckingham  
and

Lisa Renee Ivey

December, 1994

Thesis Advisor:

Xavier K. Maruyama

Approved for public release; distribution is unlimited.

19950427 031

DTIC COLLECTED 5

REPORT DOCUMENTATION PAGE			Form Approved OMB No. 0704-0188	
Public reporting burden for this collection of information is estimated to average 1 hour per response, including the time for reviewing instruction, searching existing data sources, gathering and maintaining the data needed, and completing and reviewing the collection of information. Send comments regarding this burden estimate or any other aspect of this collection of information, including suggestions for reducing this burden, to Washington Headquarters Services, Directorate for Information Operations and Reports, 1215 Jefferson Davis Highway, Suite 1204, Arlington, VA 22202-4302, and to the Office of Management and Budget, Paperwork Reduction Project (0704-0188) Washington DC 20503.				
1. AGENCY USE ONLY (Leave blank)		2. REPORT DATE December, 1994		3. REPORT TYPE AND DATES COVERED Master's Thesis
4. TITLE AND SUBTITLE EFFECTS OF MOSAICITY ON PARAMETRIC X-RADIATION PRODUCTION			5. FUNDING NUMBERS	
6. AUTHOR(S) Buckingham, William M. and Ivey, Lisa R.				
7. PERFORMING ORGANIZATION NAME(S) AND ADDRESS(ES) Naval Postgraduate School Monterey CA 93943			8. PERFORMING ORGANIZATION	
9. SPONSORING/MONITORING AGENCY NAME(S) AND ADDRESS(ES)			10. SPONSORING/MONITORING	
11. SUPPLEMENTARY NOTES The views expressed in this thesis are those of the author and do not reflect the official policy or position of the Department of Defense or the U.S. Government.				
12a. DISTRIBUTION/AVAILABILITY STATEMENT Approved for public release; distribution is unlimited.			12b. DISTRIBUTION CODE	
13. ABSTRACT (maximum 200 words)  <p>Previous measurements of parametric x-radiation (PXR) spectra from mosaic graphite observed yields that greatly exceeded theoretical predictions. At the Bragg scattering condition, the interaction of relativistically charged particles and the atomic planes of a crystal produces scattering of virtual photons. This is known as PXR. The discrepancies between actual yields and theoretical predictions might possibly have been caused by the mosaic spread of the atomic planes of the crystal. Re-analysis of previous data has shown a miscalculation of the effective target thickness used in earlier work. There was also an error in the calculation of the theory that was used for comparison. Correction of the two errors brought the data and theory in closer agreement, but the mosaic spread does change the intensity of the PXR.</p> <p>In this thesis, three samples of thick mosaic carbon graphite crystal with differing mosaic spreads are compared to determine the effect of the mosaicity on PXR yield. By obtaining "rocking curves" where the target orientation angle is changed with respect to the incident electron beam and observation angle, it was found that the mosaic spread does have an effect on the PXR spectral distribution. This effect is quite significant and can be seen when viewing the "rocking curves" of the samples. As the mosaicity is increased, the angular distribution was spread out and the coherence condition was relaxed.</p>				
14. SUBJECT TERMS parametric x-radiation, rocking curves, mosaic spread			15. NUMBER OF PAGES 89	
			16. PRICE CODE	
17. SECURITY CLASSIFICATION OF REPORT Unclassified	18. SECURITY CLASSIFICATION OF THIS PAGE Unclassified	19. SECURITY CLASSIFICATION OF ABSTRACT Unclassified	20. LIMITATION OF ABSTRACT UL	

NSN 7540-01-280-5500

Standard Form 298 (Rev 2-98)  
Prescribed by ANSI Std Z39-18  
298-102



Approved for public release; distribution is unlimited.

**EFFECTS OF MOSAICITY ON PARAMETRIC  
X-RADIATION PRODUCTION**

by

**William M. Buckingham**  
Lieutenant, United States Navy  
B.S., University of Washington, 1987

and

**Lisa R. Ivey**  
Lieutenant, United States Navy  
B.S., University of Tennessee, 1988

Submitted in partial fulfillment  
of the requirements for the degree of

**MASTER OF SCIENCE IN PHYSICS**

from the

**NAVAL POSTGRADUATE SCHOOL**

**December 1994**

Authors: *William M. Buckingham*  
William M. Buckingham

*Lisa R. Ivey*  
Lisa R. Ivey

Approved by: *Xavier K. Maruyama*  
Xavier K. Maruyama, Thesis Advisor

*Melvin A. Piestrup*  
Melvin A. Piestrup, Second Reader

*W. B. Colson* for  
William B. Colson, Chairman, Department of Physics

Accession For	
NTIS CRA&I	<input checked="checked" type="checkbox"/>
DTIC TAB	<input type="checkbox"/>
Unannounced	<input type="checkbox"/>
Justification	
By	
Distribution /	
Availability Codes	
Dist	Avail and/or Special
<b>A-1</b>	



## ABSTRACT

Previous measurements of parametric x-radiation (PXR) spectra from mosaic graphite observed yields that greatly exceeded theoretical predictions. At the Bragg scattering condition, the interaction of relativistically charged particles and the atomic planes of a crystal produces scattering of virtual photons. This is known as PXR. The discrepancies between actual yields and theoretical predictions might possibly have been caused by the mosaic spread of the atomic planes of the crystal. Re-analysis of previous data has shown a miscalculation of the effective target thickness used in earlier work. There was also an error in the calculation of the theory that was used for comparison. Correction of the two errors brought the data and theory in closer agreement, but the mosaic spread does change the intensity of the PXR.

In this thesis, three samples of thick mosaic carbon graphite crystal with differing mosaic spreads are compared to determine the effect of the mosaicity on PXR yield. By obtaining "rocking curves" where the target orientation angle is changed with respect to the incident electron beam and observation angle, it was found that the mosaic spread does have an effect on the PXR spectral distribution. This effect is quite significant and can be seen when viewing the "rocking curves" of the samples. As the mosaicity increased, the angular distribution was spread out and the coherence condition was relaxed.



## TABLE OF CONTENTS

I.	INTRODUCTION .....	1
II.	THEORETICAL BACKGROUND .....	3
III.	PXR EXPERIMENTAL DESCRIPTION .....	9
	A. ELECTRON BEAM ALIGNMENT AND STEERING .....	9
	B. SPECTROSCOPY ELECTRONICS .....	11
	C. ENERGY CALIBRATION .....	12
IV.	DATA AND ANALYSIS .....	19
	A. CALCULATION OF PXR PEAK AREAS .....	19
	B. CALCULATION OF PXR ABSOLUTE YIELD .....	28
	C. CALCULATION OF INTENSITY RATIOS .....	32
	D. CORRECTIONS TO PREVIOUS DATA .....	42
	E. ERROR ANALYSIS .....	48
V.	CONCLUSIONS AND RECOMMENDATIONS .....	57
	APPENDIX A. SAMPLE THEORETICAL YIELD PROGRAM .....	59
	APPENDIX B. SAMPLE ERROR ANALYSIS PROGRAM .....	65
	APPENDIX C. DATA VERSUS THEORY FOR ALL SAMPLES .....	67
	LIST OF REFERENCES .....	75
	INITIAL DISTRIBUTION LIST .....	77





## ACKNOWLEDGEMENTS

First and foremost, we would like to thank our thesis advisor X. K. Maruyama, for his patience which we tried on a daily basis. Without his expertise and guidance, this work would not have been possible. We would also like to remind him that great innovations come from stupid mistakes, and we made many of those.

We would also like to thank Don Snyder and Harold Rietdyk for the long late hours they spent with us during the data collection process. We also need to thank Don for repairing all of the damage we did to the computer and software during our work, including the worn out mouse.

Q. Li of the Naval Surface Warfare Center provided us with a base Mathcad program to work from for which we are very grateful. Without this, the theoretical calculations would have been very painful. We also need to express our thanks to Don Rule, also of Naval Surface Warfare Center for all of the information and calculations that he provided to us. Also, Mel Piestrup of Adelphi Technology sacrificed of himself and his time to help us and we greatly appreciate that. We would also like to wish him good luck with the new data he is collecting.

Finally, we would like to thank our families: Karen, Christopher, Alyssa, Aaron, Max, and Trey, for putting up with the long hours and our absence in the past year. For this, we dedicate this work to them.

## I. INTRODUCTION

Scattering of virtual photons produced by the interaction of a relativistic charged particle and a crystalline material at or near the Bragg condition,  $2d\sin\theta=n\lambda$ , results in the production of parametric x-radiation (PXR). [Ref. 1] This scattering is associated with the Coulomb field of the relativistic particle and the atomic planes of the crystal; in this case, a thick mosaic carbon graphite crystal was used. When the incident electron beam angle with respect to the crystal axis satisfies the Bragg condition, virtual photons are placed on the mass shell and scattered as real photons. The first PXR theory was developed by Ter-Mikaelian (1971) as resonant radiation that was produced in a thin crystal. [Ref. 1] Development of the theory for a thick crystal followed with experiments in the mid 1980's. [Ref. 2] In the early 1990's the first PXR experiments outside of the former Soviet Union were performed at Naval Postgraduate School (NPS), Monterey, California. The first experiments using a carbon target at NPS were reported in June 1992 [Ref. 3] and in December 1992. [Ref. 4] These experiments used a compression annealed pyrolytic graphite (CAPG) with a mosaic spread of  $0.45^\circ$ .

The recent theoretical work has been done by Rule et al at the Naval Surface Warfare Center in Silver Spring, Maryland. [Ref. 5] This theory predicts experimental yields due to the influence of the mosaic spread in an attempt to explain the discrepancies seen between previous experiments and theories.

In this thesis, thick mosaic graphite crystals with mosaicities of  $0.45^\circ$ ,  $1.31^\circ$ , and  $2.5^\circ$  were used with a 90 MeV electron beam at a Bragg angle of  $22.5^\circ$  which yielded x-rays in the 4 to 30 keV range. Analysis of these spectra confirmed that mosaic spread does indeed have an effect on the angular distribution and coherence conditions.



## II. THEORETICAL BACKGROUND

PXR is an important source of x-rays because of the high energy photons that are produced with the relatively low electron energy requirements of the experiments. PXR is produced by the interaction of relativistically charged particles and the atomic planes of a crystal. When the Bragg condition,  $2d\sin\theta=n\lambda$ , is satisfied, virtual photons are placed on the mass shell and scatter out as real photons. Ter-Mikaelian was the first to produce a theory for PXR in a thin crystal. The first theory for a thick crystal was by Feranchuck and Ivanshin. [Ref. 6] The emitted photons spectral and angular distributions can be expressed by:

$$\frac{\partial^2 N}{\partial n_1 \partial \omega} = \frac{e^2}{2\pi} \omega L_a |g_\tau|^2 \frac{|\kappa_\tau, \omega v + \tau|^2}{\left[ (\kappa_\perp - \tau_\perp)^2 + \frac{\omega^2}{v^2} (1 - v^2) \right]^2} \left[ 1 - \exp\left(-\frac{L}{L_a}\right) \right] \delta(q), \quad (1)$$

$$\text{where } q = \frac{\omega}{v} - \sqrt{\omega^2 - \kappa^2} + \tau_z - \frac{\omega}{2} [\text{Re}(g_0) - \theta_s] \quad (2)$$

where  $N$  is the number of photons per electron,  $e$  is the electron charge,  $\theta_s$  is the multiple scattering angle,  $L_a = [\omega \text{Im}(g_0)]^{-1}$ ,  $g_0$  and  $g_\tau$  are the perpendicular and parallel Fourier components of the dielectric susceptibility,  $\tau$  is the reciprocal lattice vector,  $n_1$  is the photon index of refraction,  $\omega$  is frequency of the emitted photon,  $v$  is particle velocity,  $\kappa_\perp$  is the component of the wave vector perpendicular to the crystal plane. Feranchuck and Ivanshin also found that the number of photons per electron per solid angle per electron energy can be found using angular displacement as follows:

$$\frac{\partial^3 N}{\partial \theta_x \partial \theta_y \partial \omega} = \frac{1}{2\pi^2} \frac{e^2}{\hbar c} \frac{1}{\omega_B} |g_\tau|^2 \frac{\theta_x^2 \cos^2(2\theta_B) + \theta_y^2}{\left( \gamma^{-2} + \theta_x^2 + \theta_y^2 + |g_0| \right)} \frac{1}{16 \sin^4 \theta_B \left( \frac{\theta_x}{\tan \theta_B} - \frac{\Delta\omega}{\omega_B} \right)^2 + \rho_s^2}, \quad (3)$$

where  $\theta_x$  and  $\theta_y$  represents the angular displacement from the Bragg condition, where  $\rho_s$  is defined as  $\lambda/[L_a(\omega)2\pi]$  with  $L_a(\omega)$  is the photon absorption length,  $\omega_B$  is the frequency of the emitted photon at Bragg condition,  $\gamma$  is defined as  $1/\sqrt{1-(v/c)^2}$ ,  $\Delta\omega$  is the difference

between the emitted photon  $\omega$  and  $\omega_B$ . [Ref. 7] To obtain the angular distribution of the spectral PXR spectra, Equation (3) can be integrated over  $\omega$ .

This theory when used by DiNova [Ref. 4] yielded values of N that were much smaller than the experimental photon production rate for all spectral orders and for each angle at or near the Bragg condition for the “near field” case and values that were larger than experimental yields for the far field case. Table 1 shows a sampling of values from DiNova and the theoretical values produced by the above equation integrated over  $\omega$ . There were corrections made to the values calculated by DiNova in the value of the effective tin thickness as will be presented in the data analysis section.

Angle ( $\theta_B$ )	Near Field			Far Field		
	Data	Theory w/o Scattering	Theory w/ Scattering	Data	Theory w/o Scattering	Theory w/ Scattering
20.1°	3.80e-6	2.53e-6	2.49e-6	-	-	-
21.1°	1.36e-5	5.47e-6	5.25e-6	2.27e-6	2.059e-6	1.99e-6
21.6°	3.01e-5	1.70e-5	2.21e-5	5.46e-7	1.15e-5	9.03e-6
22.1°	4.70e-5	2.18e-5	1.51e-5	1.14e-6	1.18e-5	7.85e-6
22.6°	6.22e-5	2.18e-5	1.38e-5	4.68e-6	8.57e-6	4.949e-6
23.1°	3.82e-5	2.18e-5	1.51e-5	3.87e-6	1.18e-5	7.85e-6
23.6°	1.58e-5	1.70e-5	2.21e-5	8.74e-7	1.15e-5	9.03e-6
24.1°	8.07e-6	5.47e-6	5.25e-6	4.25e-7	2.059e-6	1.99e-6
24.6°	6.47e-6	4.26e-6	4.11e-6	3.06e-7	1.23e-6	1.21e-6
25.6°	4.76e-6	2.53e-6	2.49e-6	-	-	-

Table 1. Comparison of Past Experimental Data Corrected for Effective Tin Thickness with Theoretical Calculations.

Rule’s calculations presented at Tomsk by Rule et al [Ref. 5] convolves PXR spectral-angular distributions with Gaussian models of the mosaic tilt angle distributions and the effects of mosaic spread,  $\sigma_m$ , is brought into play. The effect of multiple scattering,  $\sigma_s$ , is also included in the following:

and the effects of mosaic spread,  $\sigma_m$ , is brought into play. The effect of multiple scattering,  $\sigma_s$ , is also included in the following:

$$\frac{\partial N_D}{\partial \omega} = \frac{1}{\pi} \frac{e^2}{\hbar c} \frac{1}{\omega_B} \frac{|X_{10}|^2}{4\rho_s \sin \theta_B \cos \theta_B} P_D\left(\frac{\Delta\omega}{\omega}, \theta_{x1}, \theta_{x2}\right) Q_D\left(\frac{\Delta\omega}{\omega}, \theta_{y1}, \theta_{y2}\right), \quad (4)$$

$$\text{where } P_D \equiv \frac{1}{2} \operatorname{erf}\left(\frac{\theta_{x2} - \frac{\Delta\omega}{\omega} \tan \theta_B}{\sqrt{2}\sigma_x}\right) + \frac{1}{2} \operatorname{erf}\left(\frac{\theta_{x2} + \frac{\Delta\omega}{\omega} \tan \theta_B}{\sqrt{2}\sigma_x}\right) \quad (5)$$

$$\text{and } Q_D \equiv \int_{-\theta_{y1}}^{\theta_{y2}} \left(\frac{\Delta\omega}{\omega} \tan \theta_B\right)^2 \frac{\cos^2 2\theta_B}{\sqrt{2\pi\sigma_y^2}} \left(\frac{\pi}{2g^2}\right)$$

$$\cdot \operatorname{Re}\left\{E(z)\left[\frac{1}{g} - \frac{\sqrt{2}z}{\sigma_y}\right] + \frac{2}{\sqrt{2\pi\sigma_y^2}}\right\} + \frac{1}{\sqrt{2\pi\sigma_y^2}} \left(\frac{\pi}{2}\right) \operatorname{Re}\left\{E(z)\left[\frac{1}{g} + \frac{\sqrt{2}z}{\sigma_y}\right] - \frac{2}{\sqrt{2\pi\sigma_y^2}}\right\} d\theta_y \quad (6)$$

$$\text{where } E(z) \equiv e^{z^2} [1 - \operatorname{erf}(z)], \quad z \equiv \frac{(g + i\theta_y)}{\sqrt{2}\sigma_y} \quad (7)$$

$$\text{and } g^2 \equiv \gamma^{-2} + \left(\frac{\Delta\omega}{\omega} \tan \theta_B\right)^2 + |\chi_0| \quad (8)$$

with  $\sigma_x^2 = \sigma_y^2 = \sigma_m^2 + \sigma_s^2$  used to add the mean square mosaic tilt angle to the mean square scattering angle.  $\theta_{x1}$ ,  $\theta_{x2}$ ,  $\theta_{y1}$  and  $\theta_{y2}$  are the limits of integration and in this case are all equal to the radius of the circular detector aperture in radians,  $\omega_B(n) = n\pi c/d\sin(\theta_B)$  where  $d$  is the interplanar spacing,  $\gamma$  is the Lorentz factor,  $\chi_0$  is the mean dielectric susceptibility, and  $\chi_{10}$  is the dielectric structure factor. This theory appears to more accurately support the experimental results obtained.

The effects of finite aperture size must be considered when working with PXR. These effects depend on the aperture area and the distance between the target and the detector. From the above, the solid angle of view for the detector can be determined and

this can be used to determine how much of the PXR is actually being viewed by the detector.

There are two regions for a finite detector aperture called the narrow line limit regime and the aperture limited bandwidth regime. [Ref. 4] For the first case,  $\Delta\theta_x \approx p_s$ . For the second case,  $\Delta\theta_x \gg p_s$  and the distribution can be approximated as

$$\frac{\partial N}{N} \propto \Delta\theta_x J_2(u) \text{ for } -\overline{\theta_x} < \theta_x < \overline{\theta_x} \quad (9)$$

and is equal to zero otherwise. Where

$$J_2(u) = \cos^2(2\theta_B) u^2 \left[ \frac{\alpha_y}{1+u^2} \frac{1}{\alpha_y^2 + 1 + u^2} + \tan^{-1} \left( \frac{\alpha_y}{1+u^2} \right) \frac{1}{(1+u^2)^{3/2}} \right] \\ + \left[ \tan^{-1} \left( \frac{\alpha_y}{(1+u^2)^{1/2}} \right) \frac{1}{(1+u^2)^{1/2}} - \frac{\alpha_y}{\alpha_y + 1 + u^2} \right] \quad (10)$$

$$\text{and } \alpha_y = \frac{\theta_y}{\theta_{ph}} \text{ where} \quad (11)$$

$\theta_{ph} \equiv m^2/E^2 + \theta_s^2 + |g_0|$ . This is the regime with which this thesis will be concerned.

Within this regime, the "near field" is defined as  $\Delta\theta_x > \text{FWHM of } J_2(u)$  and the "far field" is defined by  $\Delta\theta_x < \text{FWHM of } J_2(u)$ . The "near field" and "far field" cases are presented in Figures (1) and (2), respectively. For this thesis, the experiments were done in the "near field", however, there are some references to previous "far field" experiments and results. As can be seen in Figure (1), in the "near field" there is very little finite aperture effects and most of the PXR is within the field of view of the detector. On the other hand, care must be taken in the analysis of the "far field" data as a large portion of the PXR is out of the view of the detector due to its limited solid angle size.



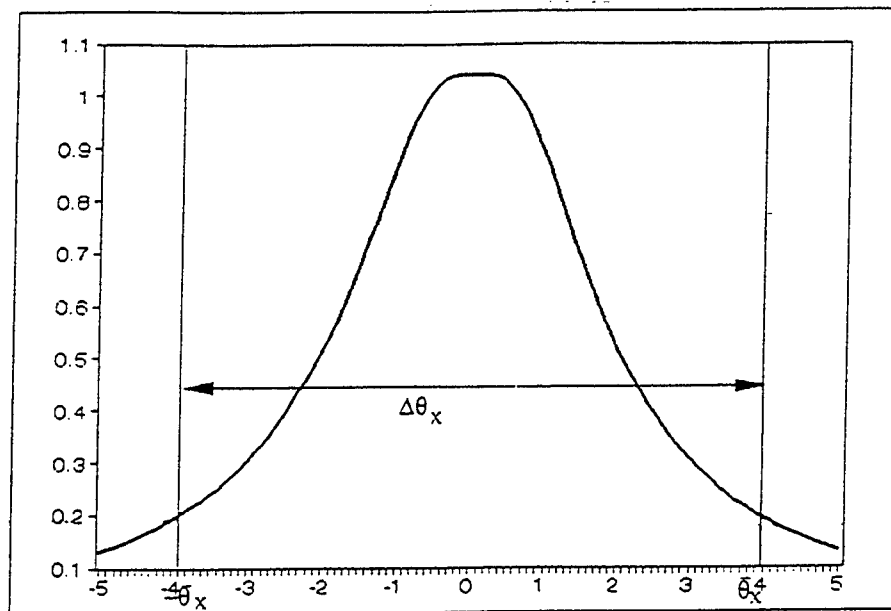


Figure 1 .  $J_2$  and the field of view for the "near field" case.

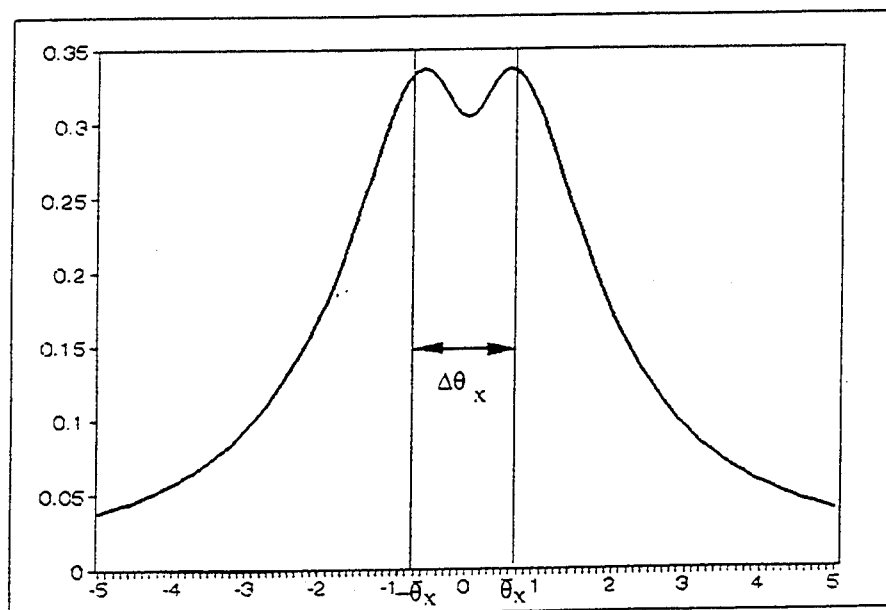


Figure 2 .  $J_2$  and the field of view for the "far field" case.



### III. PXR EXPERIMENTAL DESCRIPTION

The Naval Postgraduate School Electron Linear Accelerator (LINAC) was used to accelerate dark current electrons to energies of approximately 95 MeV. [Ref. 7] These electrons then struck three separate targets of compression annealed pyrolytic graphite (CAPG) of differing mosaicities. Initial energy calibration was performed using sandwiched foils of tin (Sn) and Yttrium (Y). In order to provide in situ energy calibration and the ability to calculate photon yields [Ref. 4], a tin (Sn) foil was placed behind the samples. "Rocking curve" data was obtained by placing the target so that its crystal plane was placed at an angle of  $21^\circ$  with respect to the electron beam direction and then rotating the target in  $0.5^\circ$  increments from the electron beam until  $26^\circ$ . This allows for comparison of the relative intensities of the  $n^{\text{th}}$  order peaks between samples.

#### A. ELECTRON BEAM ALIGNMENT AND STEERING

The LINAC is shown in Figure 3. All operations are performed and monitored from the control room. Remote cameras are used in the end station to assist in obtaining proper electron beam alignment. The accelerator consists of three 10 ft. sections, each with a separate Klystron connected by waveguides. The LINAC is operated at 2856 MHz with a pulse repetition rate of 60 Hz. The beam macro structure length is approximately 1  $\mu\text{sec}$ . Thus, the LINAC duty cycle requires the ability to count at 60 MHz when a single photon is detected during each LINAC pulse. [Ref. 4] In order to satisfy the requirement for low count rate, the LINAC was adjusted during operation to maintain one count every five to ten machine macropulses. This also ensured that simultaneous counts of two photons would not appear as one count of a higher energy photon. This is of concern as PXR peaks are integral multiples of each other with respect to energy and could result in "pile up."

A reference laser and retro optics is used to position the target ladder on which all target samples are mounted. A beam is then established in the accelerator after a vacuum

is drawn in the target chamber. The quadrupole magnets are used to provide coarse steering of the electron beam towards the target. Fine adjustment of beam position is

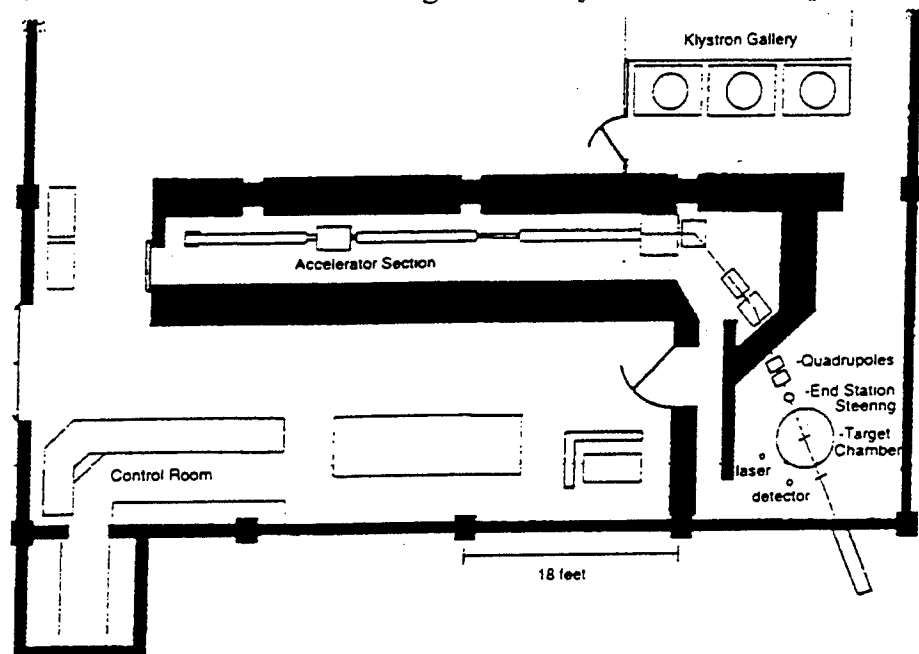


Figure 3. Overhead view of the Naval Postgraduate School 100 MeV Linear Accelerator (LINAC).

obtained by steering the beam through a small pinhole in the target ladder using the end station steering magnets.

Target chamber geometry is shown in Figure 4. The alignment laser is located  $90^\circ$  from the entrance port. The Canberra Si(Li) detector [Ref. 8] is located  $135^\circ$  from the

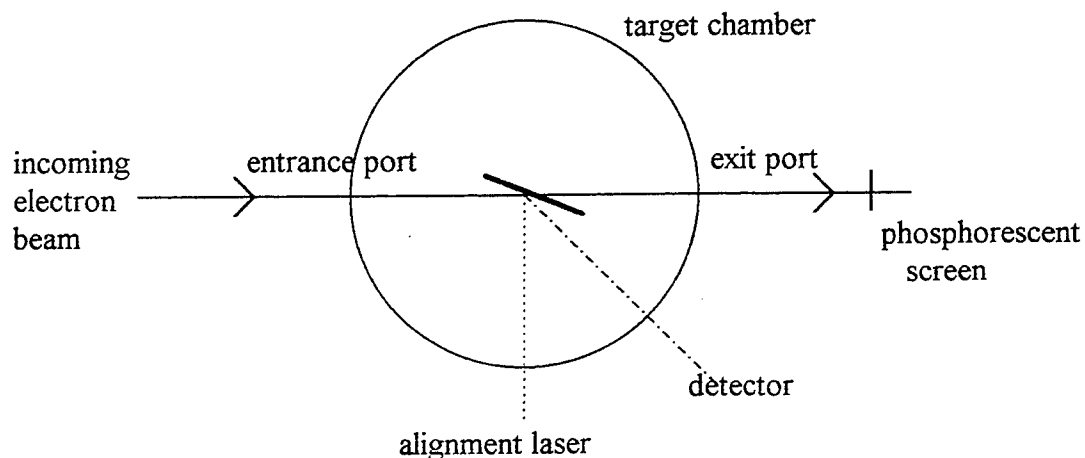


Figure 4. Overhead view of LINAC end station experimental setup.

entrance port. The target ladder could be raised and lowered remotely and it consisted of a two axis goniometer to allow rotation of the mosaic crystal. This same detector geometry was maintained for all data runs.

## B. SPECTROSCOPY ELECTRONICS

As with all detectors, the Canberra Si(Li) detector is very susceptible to ground loops as well as radiated noise from the klystrons. Thus, the end station is enclosed in a metal mesh cage to reduce the interference of radiated noise from other sources. Lead and borated polyethylene bricks were also used around the Si(Li) detector to reduce the background. Figure 5 shows the electronics setup. All system components were located in the control room with the exception of the detector and amplifier which were located in the LINAC end station.

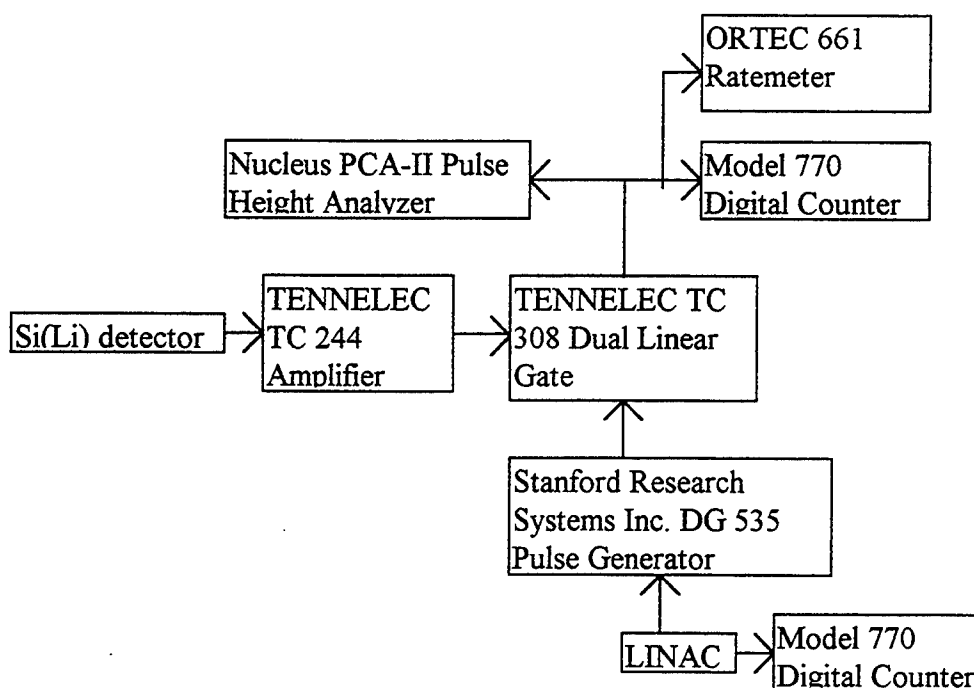


Figure 5. Electronics setup.

The signal received by the Si(Li) detector is amplified by a Tennelec TC 244 amplifier. A Tennelec TC 308 dual linear gate was used to reduce unwanted signal by providing a

25  $\mu\text{sec}$  gate during which signal could be received. This effectively made the counting system only active during the LINAC machine pulse. Triggering of the gate was performed using a Stanford Research System Inc. model DG 535 digital delay/pulse generator. By introducing a delay time ( $T_D$ ) with respect to the machine's start sequence time ( $T_0$ ), the gate was adjusted to coincide with the arrival of the beam pulse, thus,  $T_D$  was adjusted to 46  $\mu\text{sec}$ .

Another problem inherent in energy calibration of the spectra is the affect of klystron noise on the signal. The LINAC produces 60 pulses of one microsecond duration every 60 seconds. This gating has no effect on the calibration spectrum and assists in limiting noise which is non-coincident with PXR and Sn fluorescence production. On the other hand, klystron noise adds a negative bias to the received detector signal which produces a negative bias to the calibration curve if one relies solely on radioactive sources for energy calibration. Figure 6 shows the klystron noise signal in relation to detection system gating. For this reason, calibration spectra were taken prior to each day's data run using Sn and Y to eliminate this potential source of error.

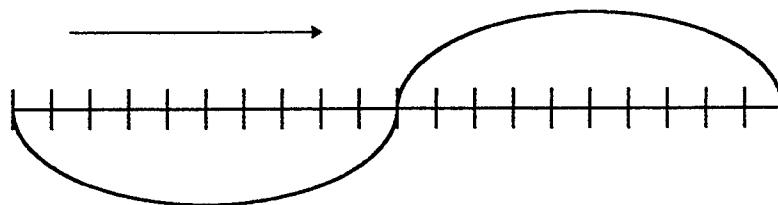


Figure 6. Representative Shape of Klystron Noise During PXR Data Collection. Line Indicates Approximate Gated Portion.

### C. ENERGY CALIBRATION

During the initial energy calibration conducted each day prior to the rocking curves, the LINAC was operated at full gun grid voltage. The beam strikes sandwiched foils of tin (Sn) and Yttrium (Y) in order to observe the  $K_\alpha$  and  $K_\beta$  fluorescent lines. Energy of the Y  $K_\alpha$  is 14 957 keV and the energies of the Sn  $K_\alpha$  and  $K_\beta$  lines are

25.270 keV and 28.483 keV respectively. [Ref. 9] PCA-II pulse height analyzing software [Ref. 10] was used to ensure calibration of all 512 channels. "Rocking curve" data was then taken beginning at 21.0° from the electron beam and proceeding in 0.5° increments to 26.0° with the LINAC operating at dark current. This is required in order to limit the photon count rate since the photon detector, a Canberra model SI200250 Si(Li) detector, has a resolution time of 12  $\mu$ sec determined by the pulse shaping preamplifier. Dark current is the term used to describe operation of the LINAC with no gun grid voltage applied. Thus, only stray electrons are accelerated toward the target crystal.

In order to provide in situ energy calibration, a tin (Sn) foil was placed behind each CAPG sample. Table 2 provides target and tin (Sn) thickness for each sample. Each thickness measurement was obtained by taking the average of five thickness measurements at different positions on the sample. Each target crystal has a density ( $\rho$ ) of  $2.260 \pm 0.005$  grams per cubic centimeter. The {002} reflecting plane spacing is  $3.356 \pm 0.003$  Angstroms.

The Union Carbide specifications for the mosaicities of the samples were  $0.4 \pm 0.1^\circ$ ,  $1.2 \pm 0.2^\circ$ , and  $3.5 \pm 1.5^\circ$ . Since the tolerances from the prescribed mosaic spread were quite large, the samples were sent to Naval Surface Warfare Center (NSWC) for determination of the actual mosaic spreads. This was measured with an x-ray diffractometer. The resulting spectra from the x-ray diffraction are presented in Figures 7 through 9. [Ref. 11] For each sample, the mosaic spread was determined by the full width at half maximum (in degrees) of these curves. The resulting spreads were  $0.45^\circ$ ,  $1.2^\circ$ , and  $2.5^\circ$ .

<b>Mosaic Spread</b>	<b>0.45°</b>	<b>1.31°</b>	<b>2.5°</b>
<b>Target Thickness</b>	$1389 \pm 1 \mu\text{m}$	$1659 \pm 1 \mu\text{m}$	$1789 \pm 1 \mu\text{m}$
<b>Sn Thickness</b>	$152 \pm 1 \mu\text{m}$	$154 \pm 1 \mu\text{m}$	$156 \pm 1 \mu\text{m}$

Table 2. Sample and Sn Thickness for each Sample.

Energies (in keV) for each channel were established during the calibration runs by the PCA-II pulse height analyzing software using the following equation:

$$E = a_0 + a_1(\text{channel}) + a_2(\text{channel})^2 \quad (12)$$

where  $a_0$ ,  $a_1$  and  $a_2$  are constants determined by performing Gaussian fits of the counts received in each region of interest surrounding the Yt and Sn calibration peaks. These constants for each series of data is shown in Table 3. The energy calibration was verified by comparing the  $K_\alpha$  and  $K_\beta$  lines produced by the Sn backing used during each PXR data run against the known value. Good agreement was observed for all PXR spectral data.

Mosaic Spread	0.45°	1.31°	2.5°
$a_0$	1.95	1.86	1.34
$a_1$	0.0722	0.0712	0.0764
$a_2$	0	0	8.53e-6

Table 3. Calibration Constants for each Sample.



## Rocking Curve Mosaic Graphite ZYA

Copper  $K\alpha$  ( 8 keV )

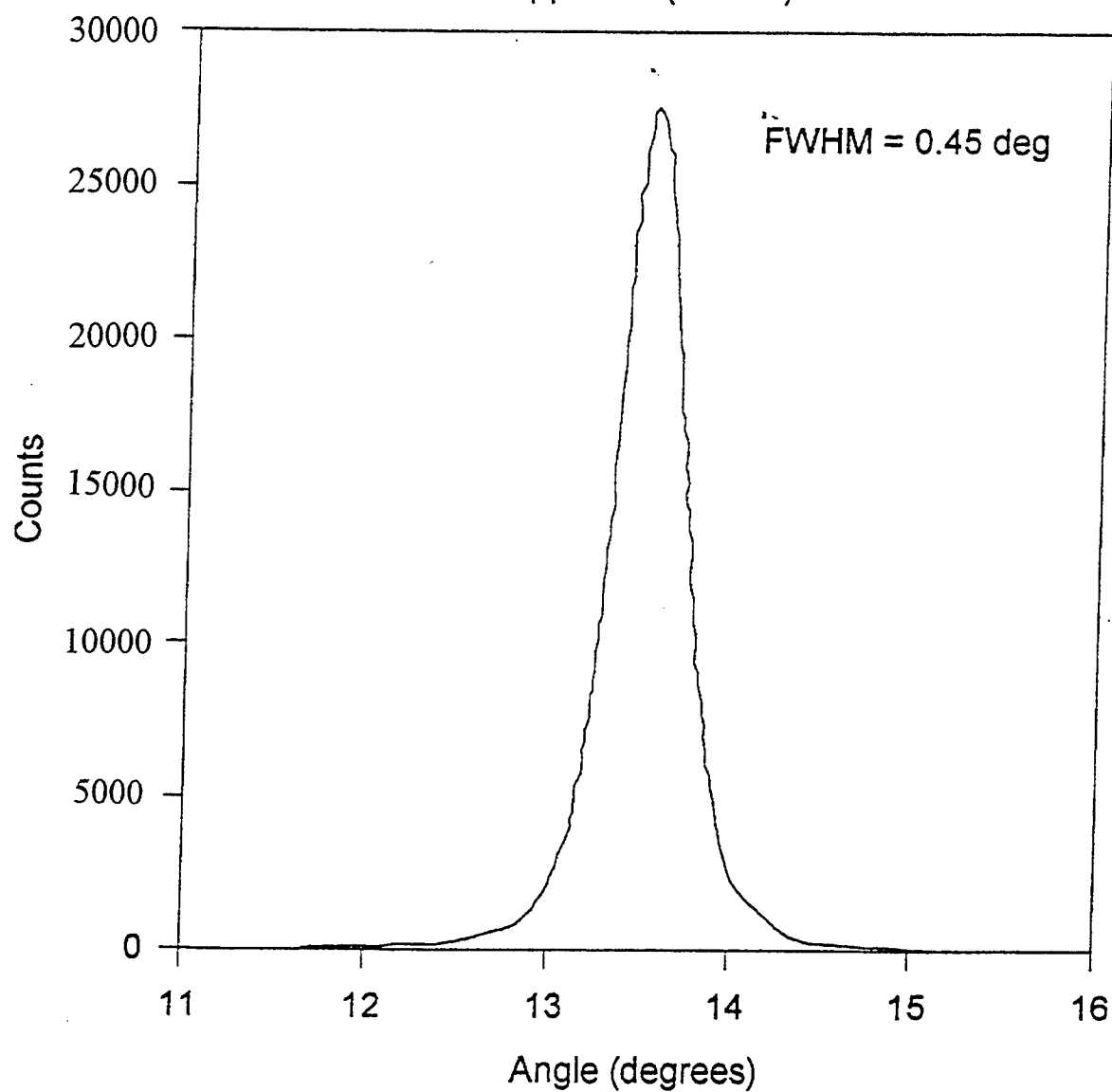


Figure 7. Mosaicity Measurement curve for 0.45° Sample.

## Rocking Curve Mosaic Graphite ZYD

Copper K $\alpha$  ( 8 keV )

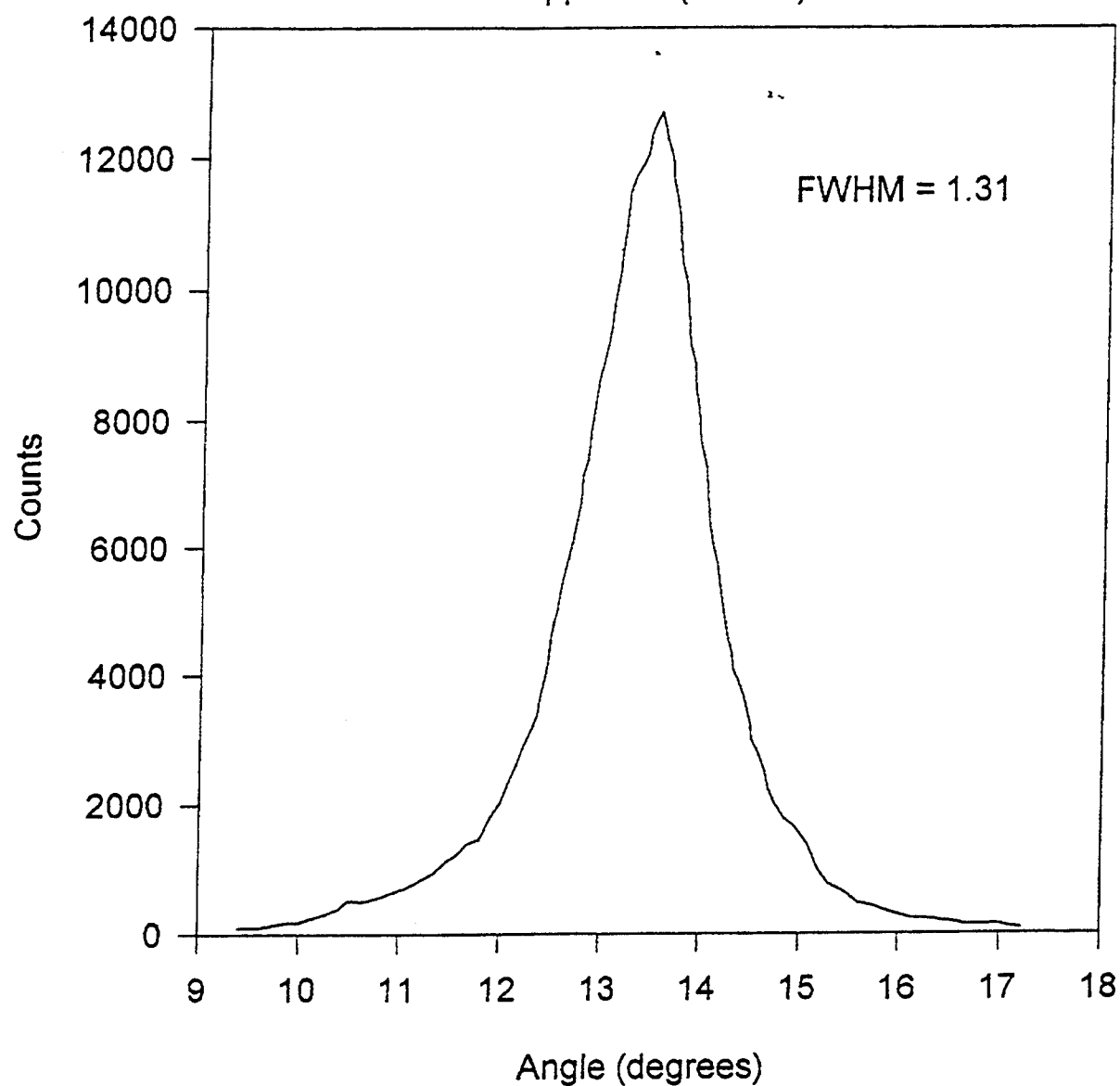


Figure 8. Mosaicity Measurement curve for 1.31° Sample.

# Rocking Curve Mosaic Graphite ZYH

Copper K $\alpha$  ( 8 keV )

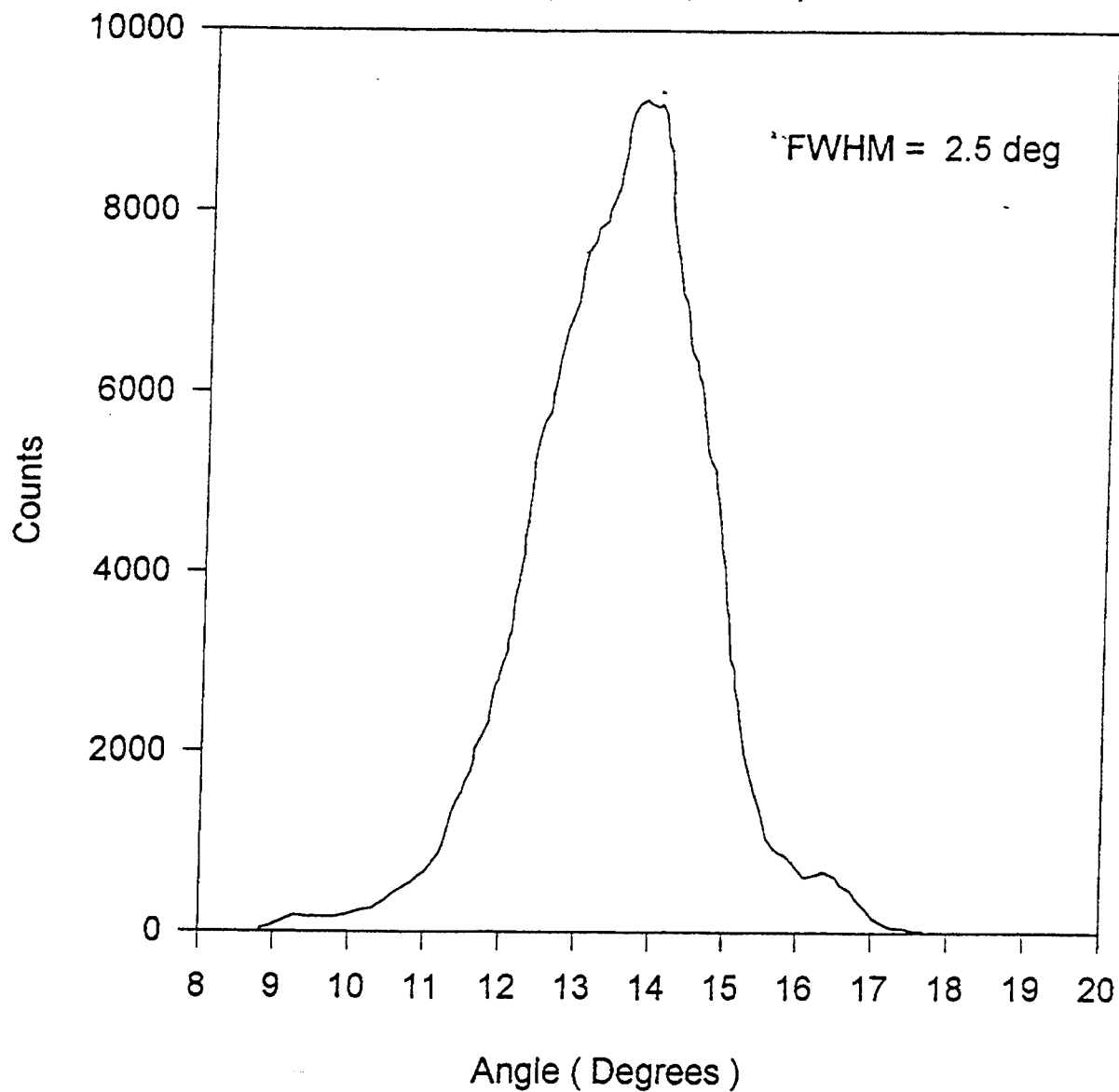


Figure 9. Mosaicity Measurement curve for 2.5° Sample.



## IV. DATA AND ANALYSIS

### A. CALCULATION OF PXR PEAK AREAS

The data from the detector was collected using a PCA-II pulse height analyzer [Ref. 10] in ASCII format. Raw data spectra for the  $0.45^\circ$ ,  $1.31^\circ$ , and  $2.5^\circ$  mosaic samples are shown in Figures 10, 11, and 12 respectively. Data was recorded for each sample spectrum for approximately 30 minutes with electron energies ( $E_e$ ) of 99.05 MeV, 95.32 MeV, and 97.62 MeV respectively. The spectra were then input into Quattro Pro (QPRO) spreadsheets [Ref. 12] so that it would be in proper format for the spectrum analyzing software. Peakfit v3.0 [Ref. 13] was used to remove the background noise and produce a Gaussian fit for each spectral peak. Figure 13 a) b) and c) show the uncorrected, background removed, and attenuation corrected spectrums respectively for the  $0.45^\circ$  sample at  $22.5^\circ$ . The program also integrated each peak to produce a net area for each peak and the full width at half maximum values for each peak of the spectrum. The values were placed in a Microsoft Excel worksheet [Ref. 14] and corrected for attenuation using Photcoef. [Ref. 15] Photcoef was used to calculate the attenuation coefficients for the Kapton ( $C_{22}O_5N_2H_{10}$ ) window, the Beryllium (Be) window and the air gap at each energy. Thicknesses for each of these were 0.0025 cm, 0.005 cm, and 0.5 cm respectively. At low energies, the attenuation coefficients varied across each peak. For the first peaks only, the attenuation coefficients for the left most channel, the peak center and the right most channel were added in quadrature and averaged to obtain a more accurate correction for the peak. For the higher order peaks, the attenuation coefficients were approximately constant across the peak and the coefficient was obtained for the

center channel of the peak and applied to the entire peak. The areas were then corrected to account for these attenuations as follows:

$$N_0 = N * e^{[(\mu\rho t)_{Be} + (\mu\rho t)_{Air} + (\mu\rho t)_{Kapton}]} \quad (13)$$

where  $N_0$  is the total number of photons before attenuation,  $N$  is the total number of photons after attenuation,  $\mu$  is the attenuation coefficient,  $\rho$  is the density of the attenuating medium, and  $t$  is the distance travelled in the attenuating medium. The efficiency of the detector had to also be accounted for in the corrections. The efficiency curve for the Canberra detector at various energies can be found in Figure 14. [Ref. 8]

# 0.45° MOSAICITY SPECTRA

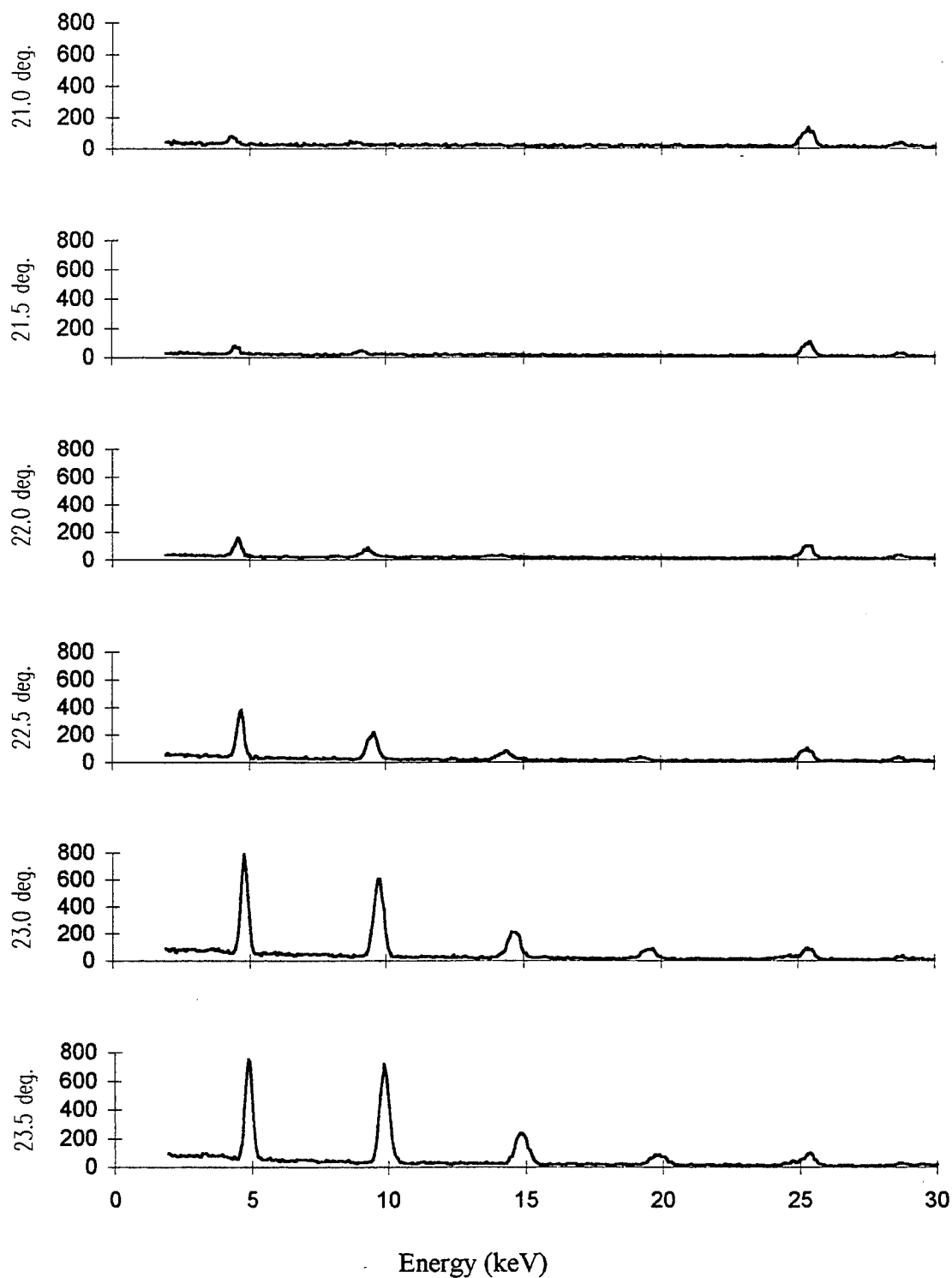


Figure 10. Raw 0.45° Mosaicity Spectra at  $E_e = 99.05$  MeV

### 0.45° MOSAICITY SPECTRA (CONT.)

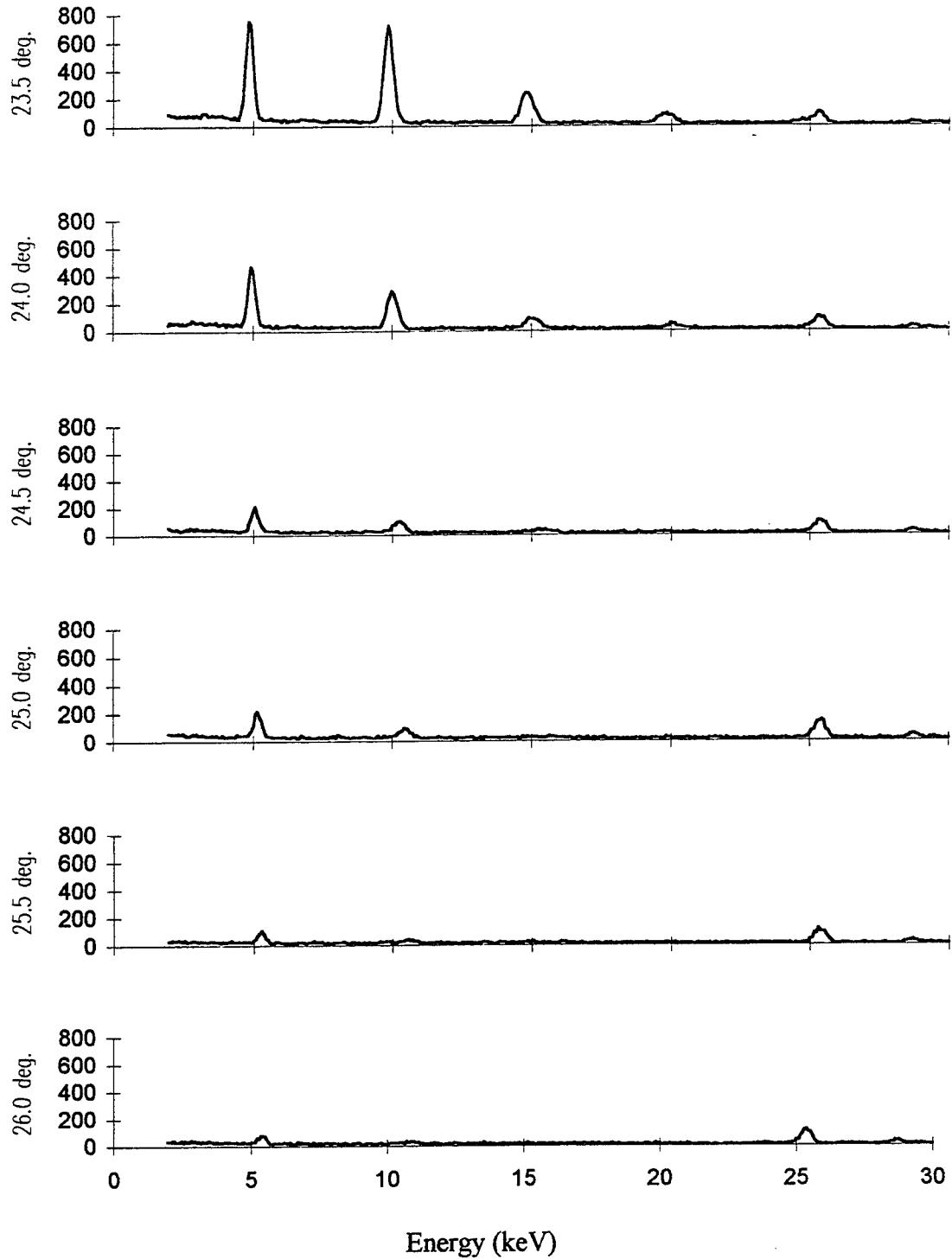


Figure 10. Raw 0.45° Mosaicity Spectra at  $E_e = 99.05$  MeV (Cont.).



### 1.31° MOSAICITY SPECTRA

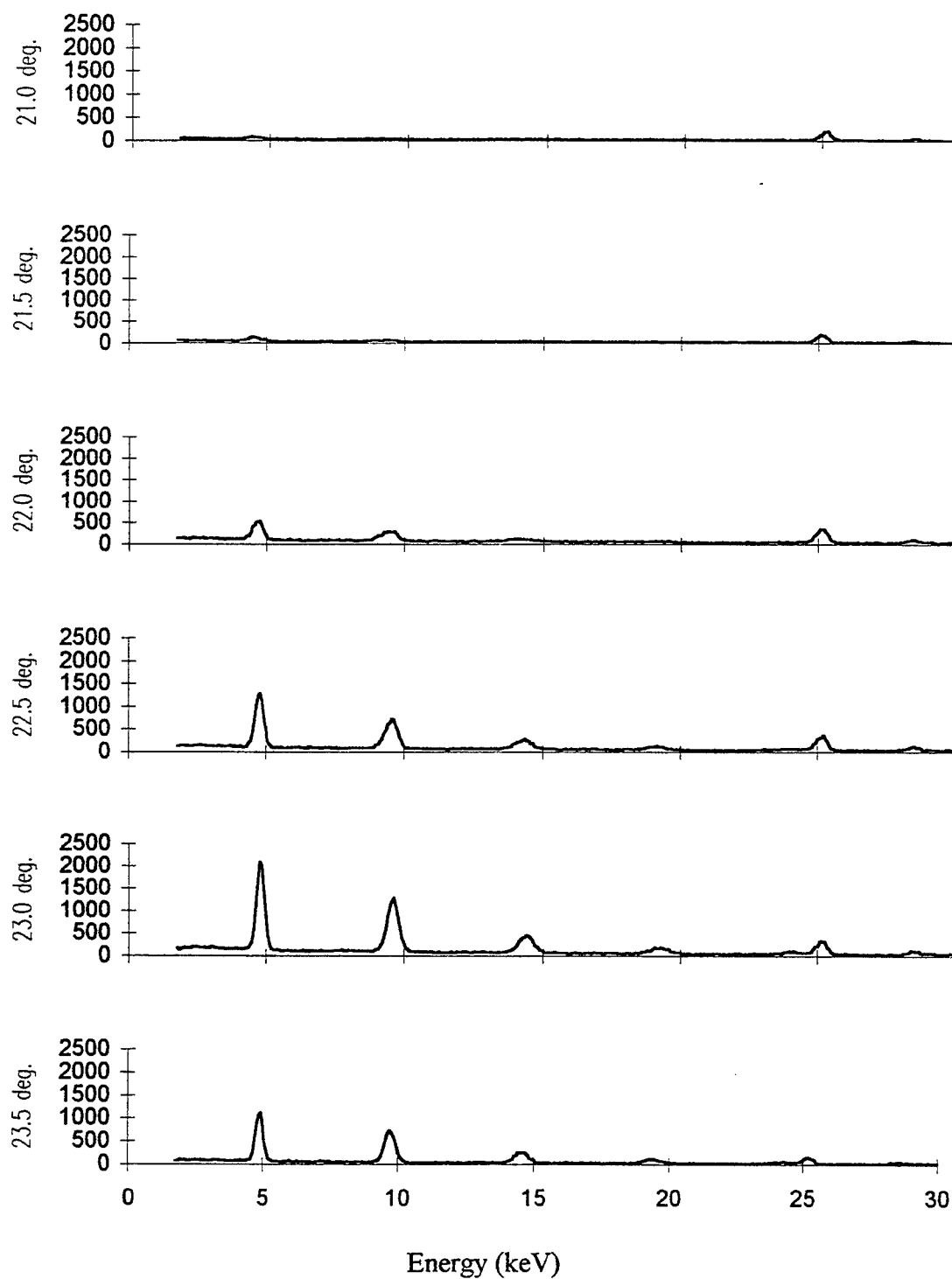


Figure 11. Raw 1.31° Mosaicity Spectra at  $E_e = 95.32$  MeV.

### 1.31° MOSAICITY SPECTRA (CONT.)

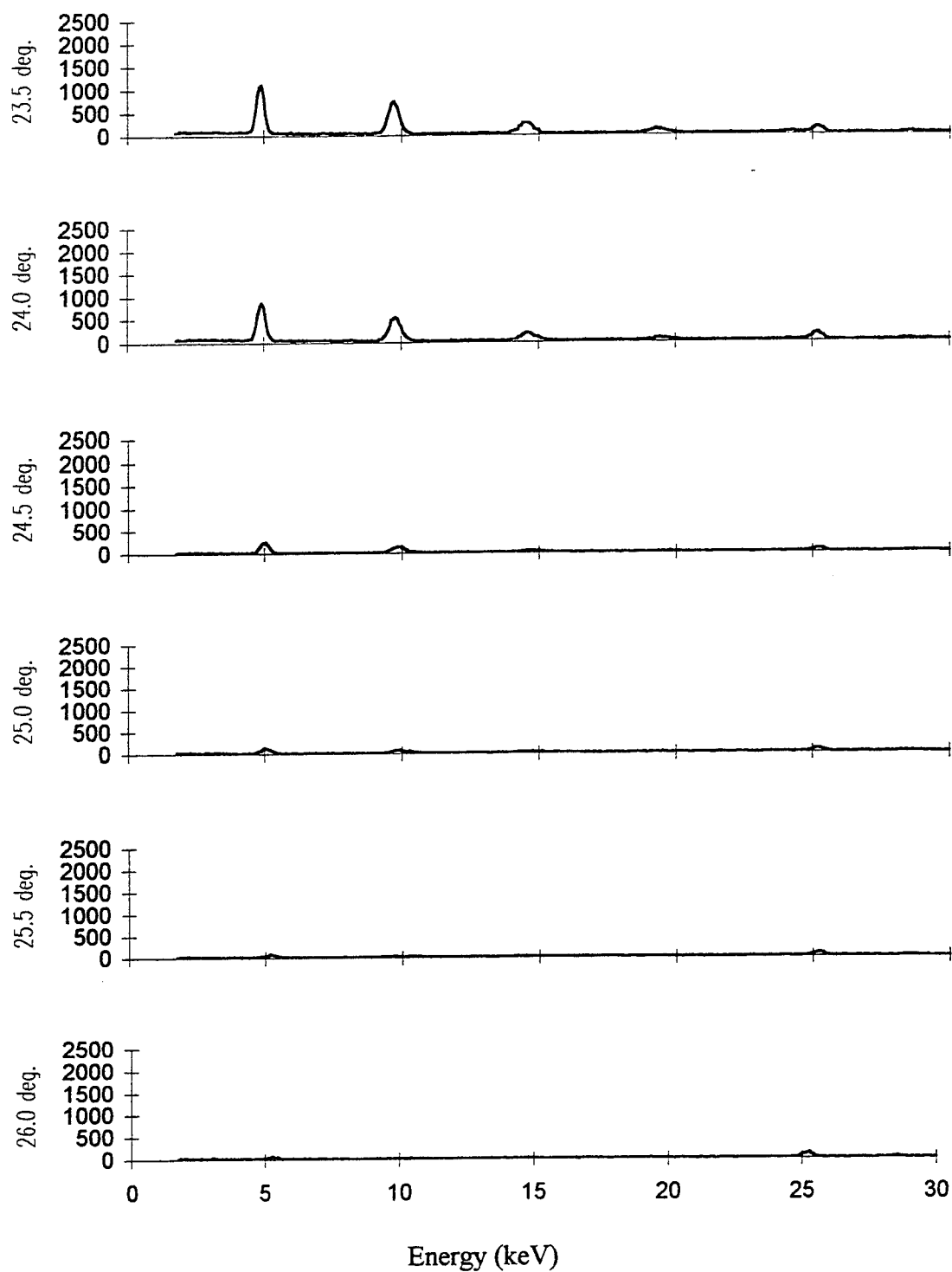


Figure 11. Raw 1.31° Mosaicity Spectra at  $E_e = 95.32$  MeV(Cont.).

## 2.5° MOSAICITY SPECTRA

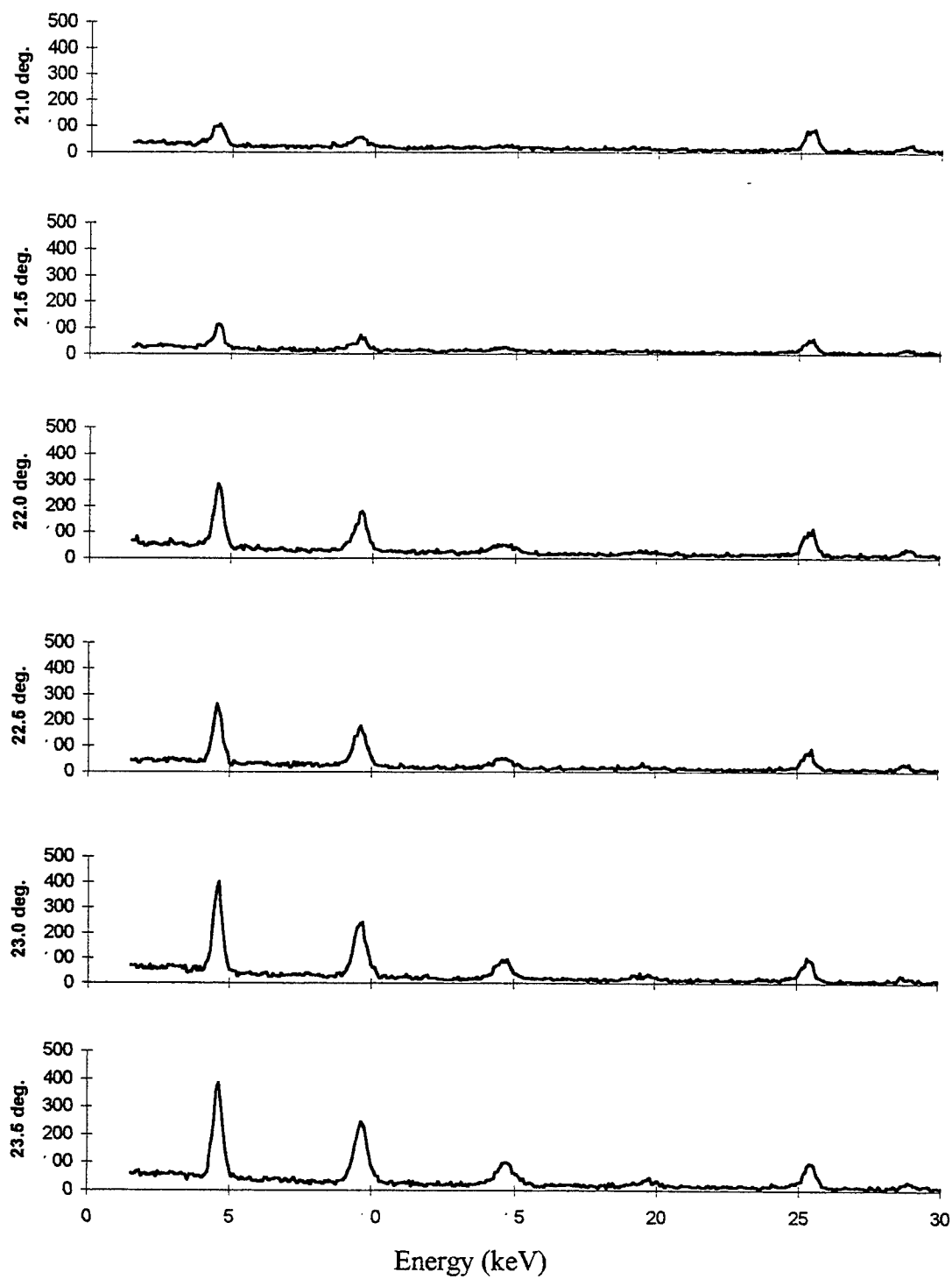


Figure 12 Raw 2.5° Mosaicity Spectra at  $E_c = 97.62$  MeV.

## 2.5° MOSAICITY SPECTRA (CONT.)

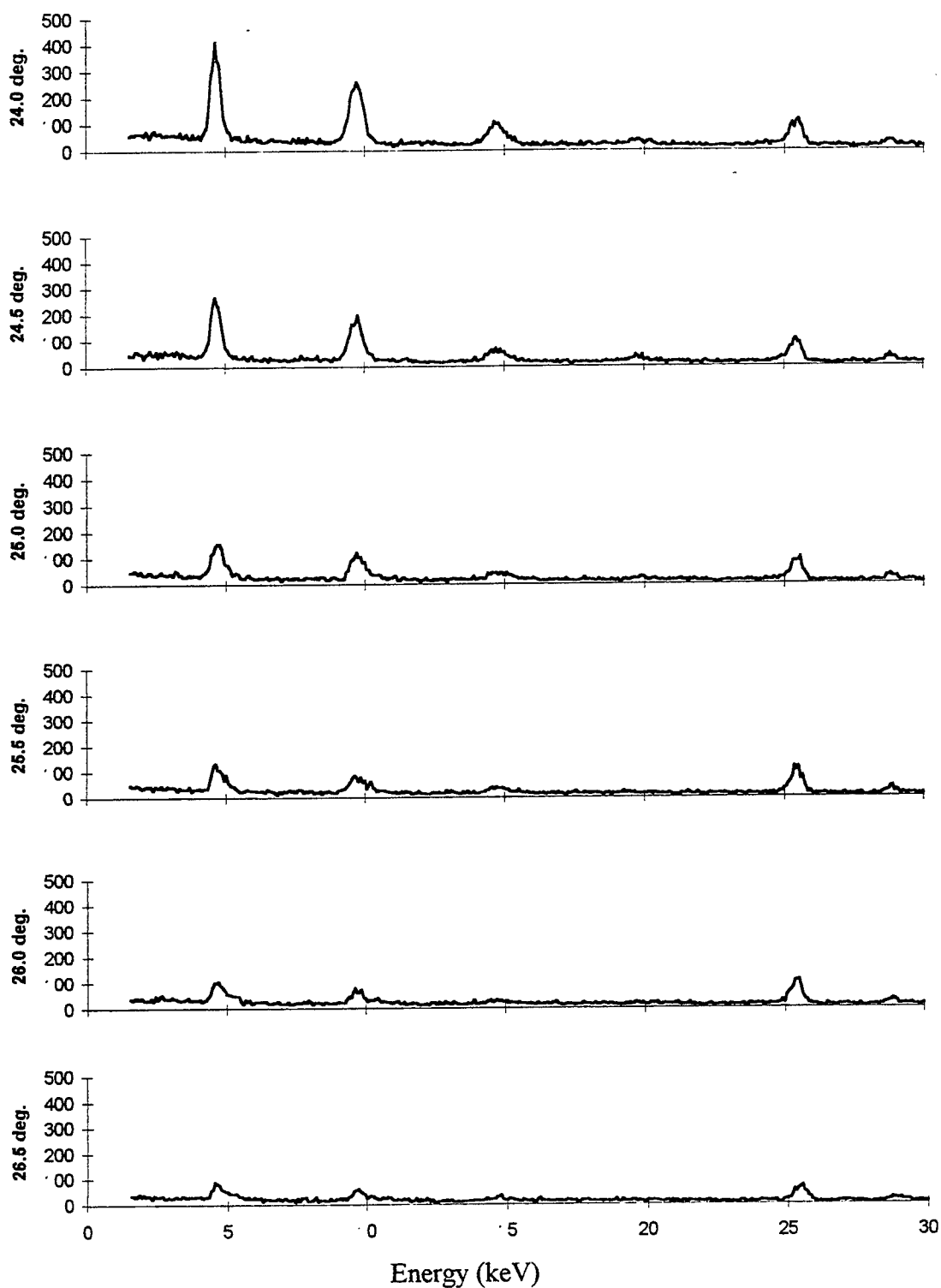


Figure 12. Raw 2.5° Mosaicity Spectra at  $E_e = 97.62$  MeV(Cont.).

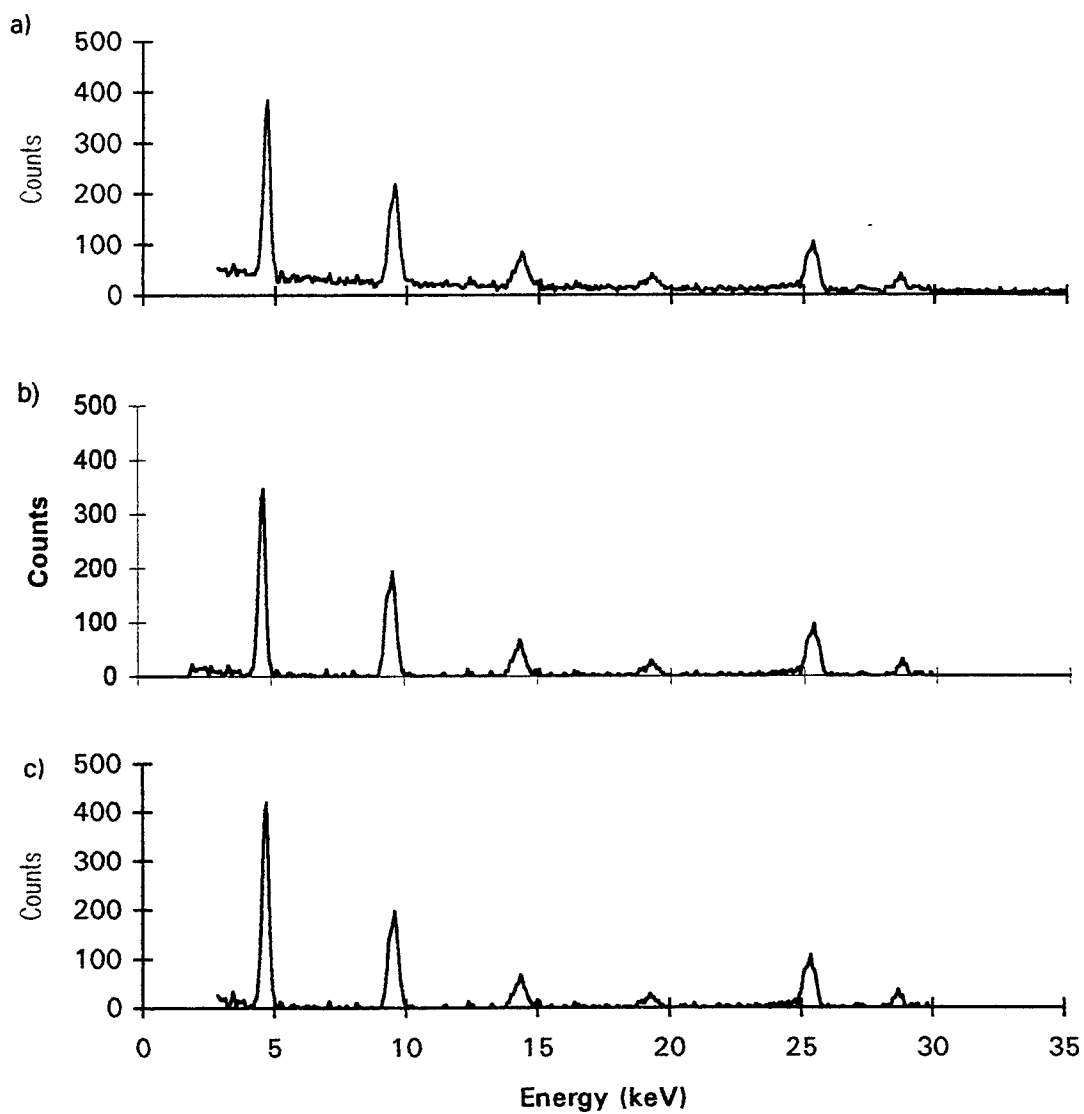


Figure 13. a) Uncorrected PXR spectrum for  $0.45^\circ$  mosaic spread at  $22.5^\circ$ . b) The same spectrum with background removed. c) Spectrum corrected for attenuation between the sample and the detector.

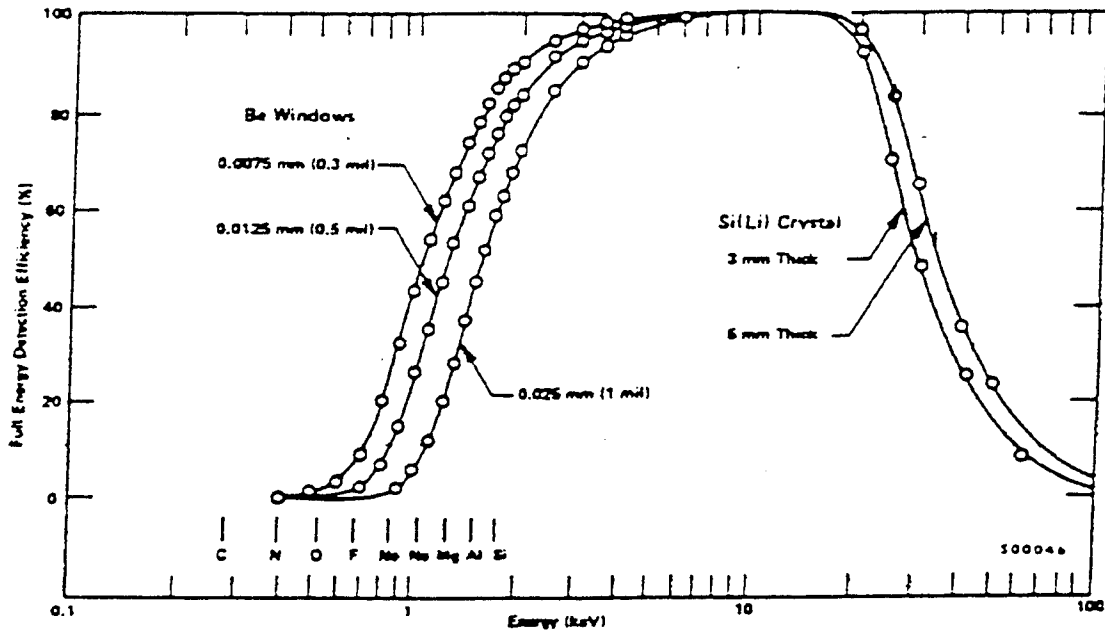


Figure 14. Efficiency Curves for Canberra Si(Li) Detector.

## B. CALCULATION OF PXR ABSOLUTE YIELD

The corrected PXR areas are then used as follows to calculate the number of photons produced for each electron.

$$I_{LINAC} = \frac{(Area_{TIN}/time)(AW_{TIN})}{\sigma_{TIN}(\Omega_{D1}/4\pi)\rho(N_A)f_{dex}(t)} \quad (14)$$

and

$$N = \frac{(Area_{PXR}/time)}{I_{LINAC}} \quad (15)$$

Combining Equations 14 and 15 yields:

$$N = \frac{Area_{PXR}\sigma_{TIN}\frac{\Omega_{det}}{4\pi}\rho N_a f_{dex}t}{(Area_{TIN})AW_{TIN}} \quad (16)$$

where  $\text{Area}_{\text{PXR}}$  and  $\text{Area}_{\text{TIN}}$  are the integrated intensities of the respective peaks, corrected for both attenuation and detector efficiency,  $\text{AW}_{\text{TIN}}$  is the atomic weight of tin  $\sigma$  is the electron interaction cross section ( $1.0\text{e-}26 \text{ m}^2$ ) [Ref. 16].  $\Omega_{\text{det}}$  is the detector solid angle ( $4.15\text{e-}4 \text{ sr.}$ ),  $f_{\text{dex}}$  is the de-excitation transition probability (0.712) [Ref. 17], and  $t$  is the effective tin thickness. The effective thickness used in the above equation was calculated by dividing the thickness of the tin ( $t_{\perp}$ ) by the sine of the angle of incidence of the electron beam. The thickness of the tin ( $t_{\perp}$ ) was  $152 \pm 1 \text{ }\mu\text{m}$ ,  $154 \pm 1 \text{ }\mu\text{m}$ , and  $156 \pm 1 \text{ }\mu\text{m}$  for the  $0.45^\circ$ ,  $1.31^\circ$ , and  $2.5^\circ$  mosaic samples respectively. The geometry of the electron beam as it strikes the Sn foil presented in Figure 15. This calculation was done for the first peak at each angle of the rocking curve for all three samples. The number of photons per electron (N) versus angle for the first and second order PXR peaks are presented in Figures 16 and 17 for each sample.

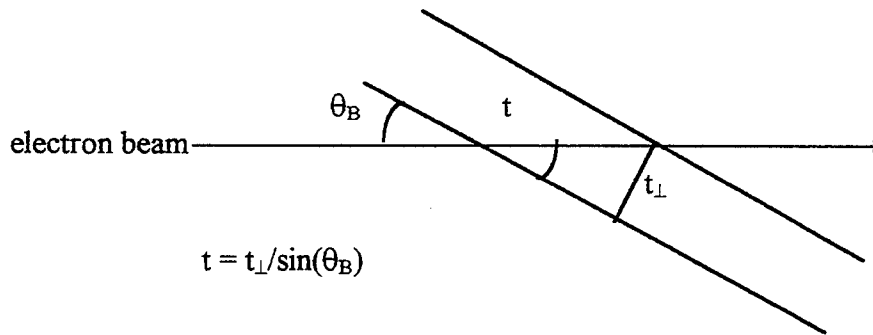


Figure 15. Configuration in Target Chamber Used to Determine Tin Effective Thickness.  $t_{\perp}$  is the Normal Target Thickness.  $\theta_B$  is the Bragg Angle or the Angle Between the Target Face and the Electron Beam Direction.

# FIRST PEAK COMPARISON

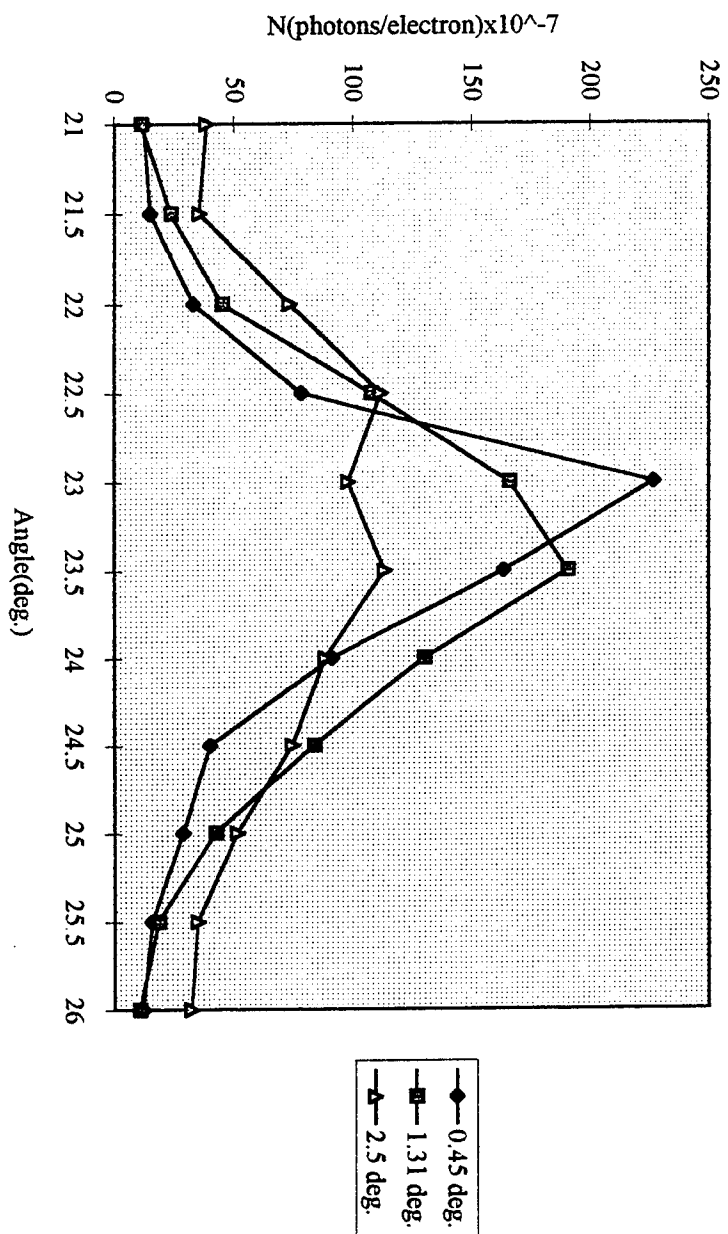


Figure 16. Comparison of Corrected First Order PXR Intensities ( $N$ ). 0.45°, 1.31°, and 2.5° Refer to the Mosaic Spread of the Graphite Targets. The Electron Energies ( $E_e$ ) are 99.05 MeV, 95.32 MeV, and 97.62 MeV Respectively.



## SECOND PEAK COMPARISON

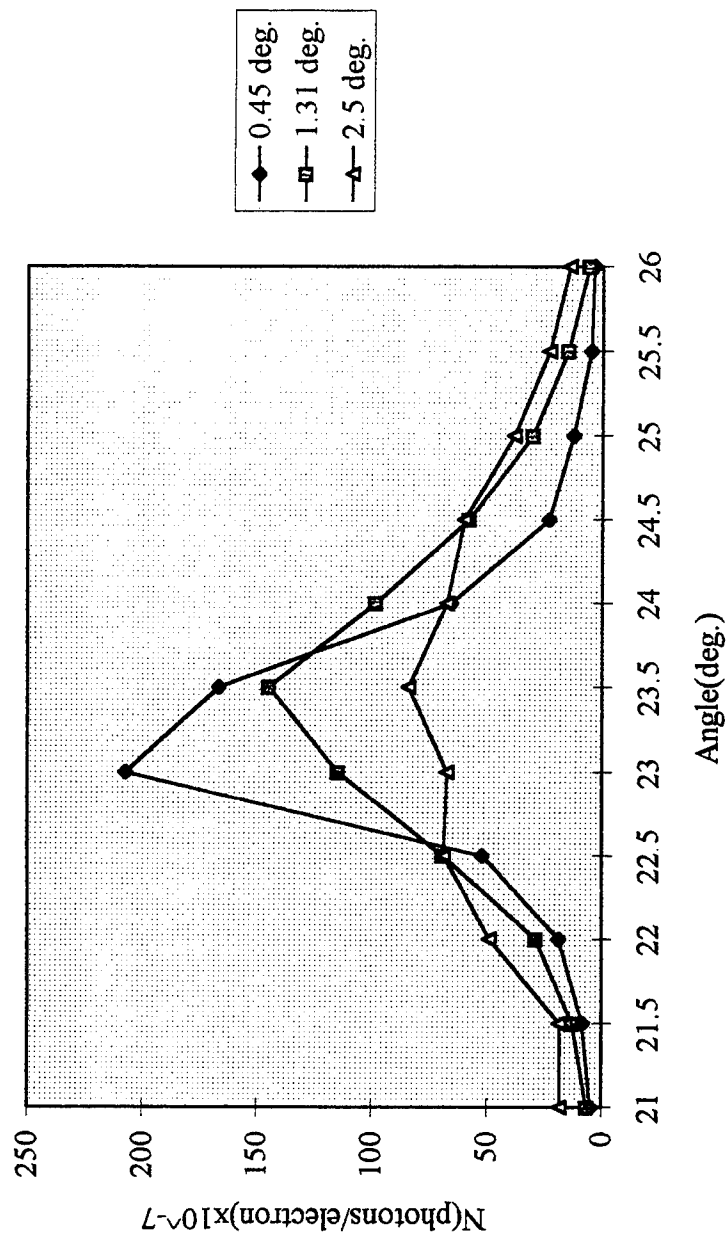


Figure 17. Comparison of Corrected Second Order PXR Intensities (N). 0.45°, 1.31°, and 2.5° Refer to the Mosaic Spread of the Graphite Targets. The Electron Energies ( $E_e$ ) are 99.05 MeV, 95.32 MeV, and 97.62 MeV Respectively.

### C. CALCULATION OF INTENSITY RATIOS

The higher order peaks were compared to the first peak absolute yield for each angle of the samples to give an intensity ratio. These calculations are presented in Table 4 and will be used for analysis of theoretical predictions. For each sample, the values presented in Figure 16 were normalized to the highest first order intensity to provide a comparison of the relative intensities of the first order PXR peaks across the “rocking curve.” These values are presented in Figure 18. The same comparison was made for the second order PXR peaks and is presented in Figure 19.

In order to provide a comparison of the data with theory for all three samples, Equation 3 was integrated over  $\omega$ ,  $\theta_x$ , and  $\theta_y$  for the solid angle subtended by the detector. These calculations are referred to here as theory without scattering. To account for multiple scattering and mosaic spread, Equation 17 was used. [Ref. 4] These calculations

$$\frac{\partial^2 N}{\partial \theta_x \partial \theta_y} = \sum_{n=1}^{\infty} \frac{e^2}{4\pi} \frac{\omega_B}{c} L_a \left[ 1 - \exp\left(-\frac{L}{L_a}\right) \right] \frac{|g_\tau(\omega_B)|^2 [\theta_x \cos^2 2\theta_B + \theta_y^2]}{\sin^2 \theta_B [\theta_x^2 + \theta_y^2 + \theta_{ph}^2]} \quad (17)$$

$$\text{where } \theta_{ph}^2 = \frac{m^2}{E^2} + \theta_s^2 + |g_0| \quad (18)$$

$$\text{and } \theta_s^2 = \theta_{multiscat}^2 + \theta_{beam-div}^2 + \theta_{mos}^2 \quad (19)$$

are referred to as theory with scattering. Appendix A shows a sample of the MathCad [Ref. 18] program used to calculate the values shown for theoretical calculations, with and without taking into account the effects of mosaic spread and multiple scattering. Figures 20 through 25 give a comparison of the data with the resulting theoretical curves for each sample, including both the first and second order PXR peaks. Agreement between the data and theory appears to break down as the mosaic spread increases. Thus, the method presented by Rule et al of convolving the PXR spectral-angular distributions with Gaussian models of the mosaic tilt angle appears to provide better agreement. Table 5 provides the theoretical intensities and ratios for the first and second order PXR peaks at Bragg condition provided by Rule for a detector solid angle of  $4.15 \times 10^{-4}$  sr. [Ref. 19] Further calculations using this model are in progress.

$\theta_B$	0.45° Mosaicity					1.31° Mosaicity				2.5° Mosaicity			
	N(2)/ N(1)	N(3)/ N(1)	N(4)/ N(1)	N(5)/ N(1)		N(2)/ N(1)	N(3)/ N(1)	N(4)/ N(1)		N(2)/ N(1)	N(3)/ N(1)	N(4)/ N(1)	
21.0°	0.38					0.57				0.47	0.11		
21.5°	0.55					0.55	0.18			0.52	0.18		
22.0°	0.57	0.19				0.63	0.22			0.67	0.28	0.12	
22.5°	0.67	0.26	0.11			0.64	0.27	0.11		0.61	0.19		
23.0°	0.91	0.39	0.17	0.09		0.69	0.29	0.12		0.69	0.27	0.13	
23.5°	1.02	0.44	0.18			0.76	0.32	0.15		0.74	0.36	0.01	
24.0°	0.72	0.27	0.11			0.76	0.29	0.12		0.77	0.30	0.11	
24.5°	0.58	0.21				0.69	0.27	0.10		0.80	0.31	0.12	
25.0°	0.44					0.72	0.24	0.11		0.74	0.32	0.10	
25.5°	0.32					0.82	0.06			0.66	0.23		
26.0°	0.30					0.56				0.44			
26.5°										0.49	0.17		

Table 4. Experimental Mosaic Sample Intensity Ratios.

# FIRST PEAK NORMALIZED

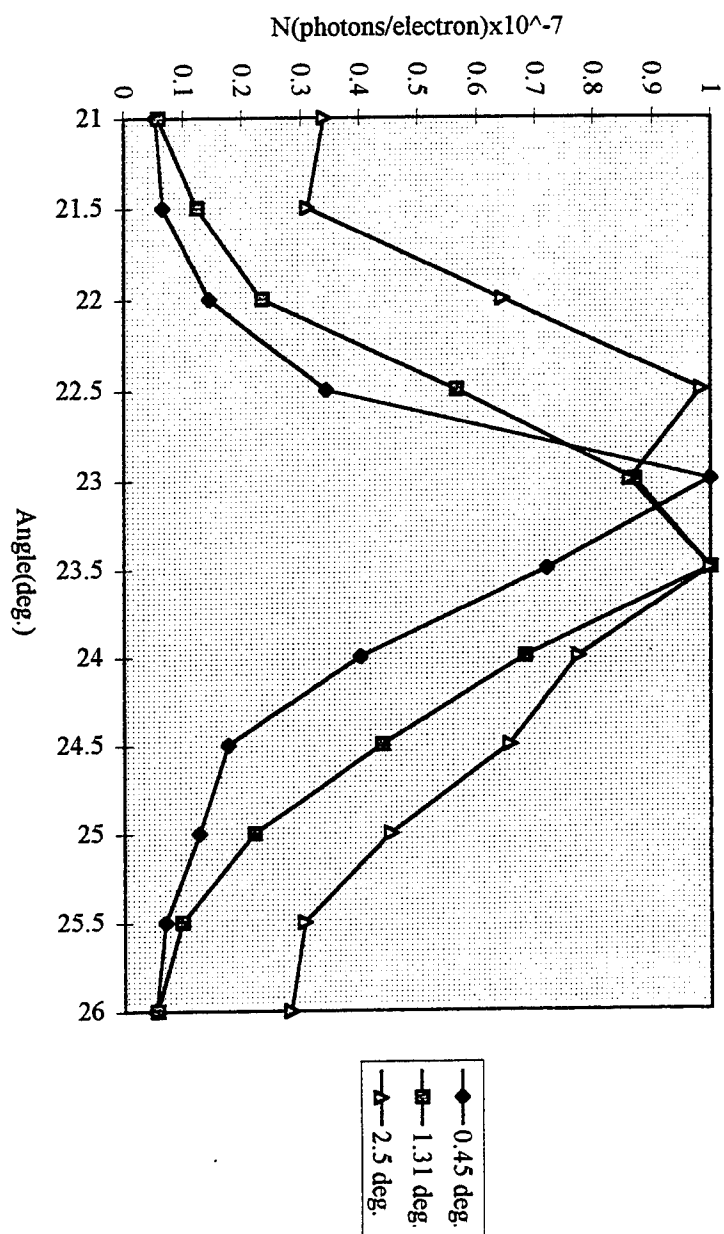


Figure 18. Comparison of Corrected First Order PXRD Intensities Normalized to the Highest Intensity for Each Sample.

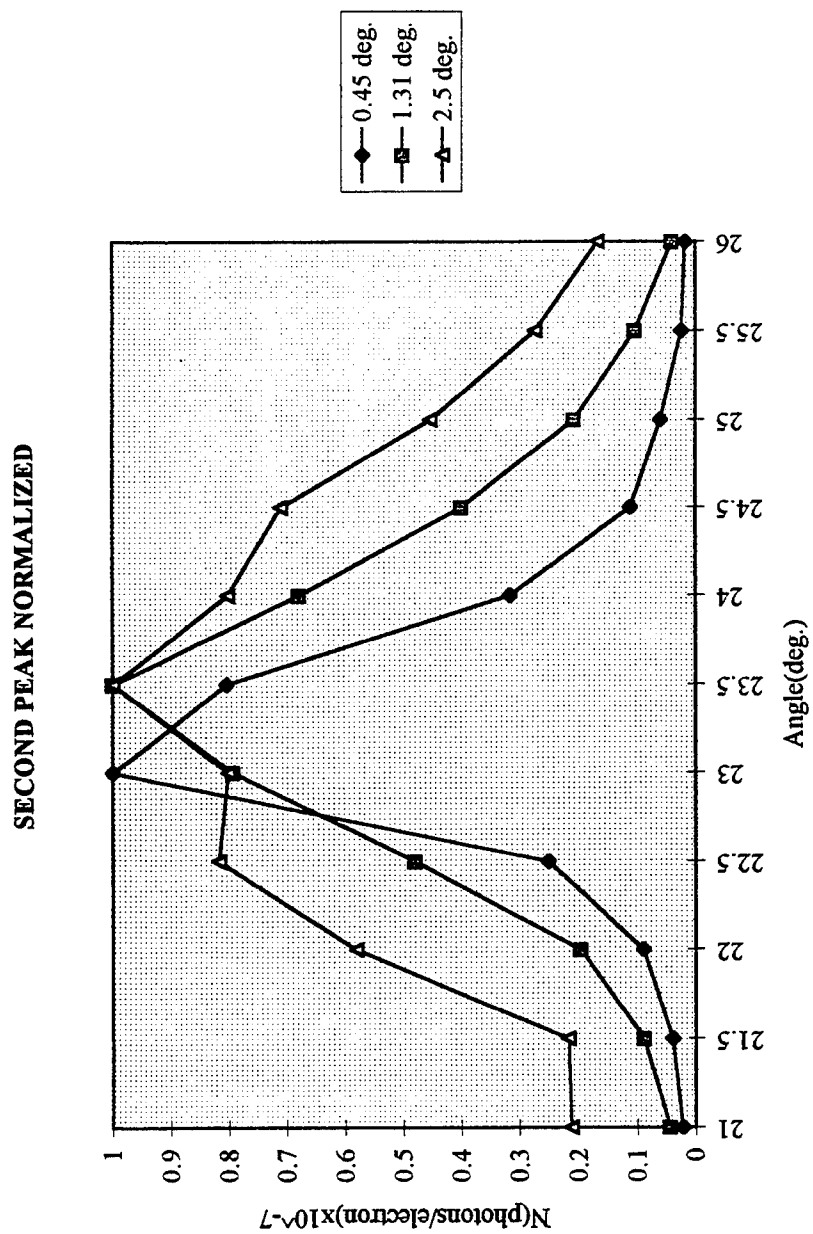


Figure 19. Comparison of Corrected Second Order PXR Intensities Normalized to the Highest Intensity for Each Sample

# 0.45 DEG. FIRST PEAK DATA VS. THEORY

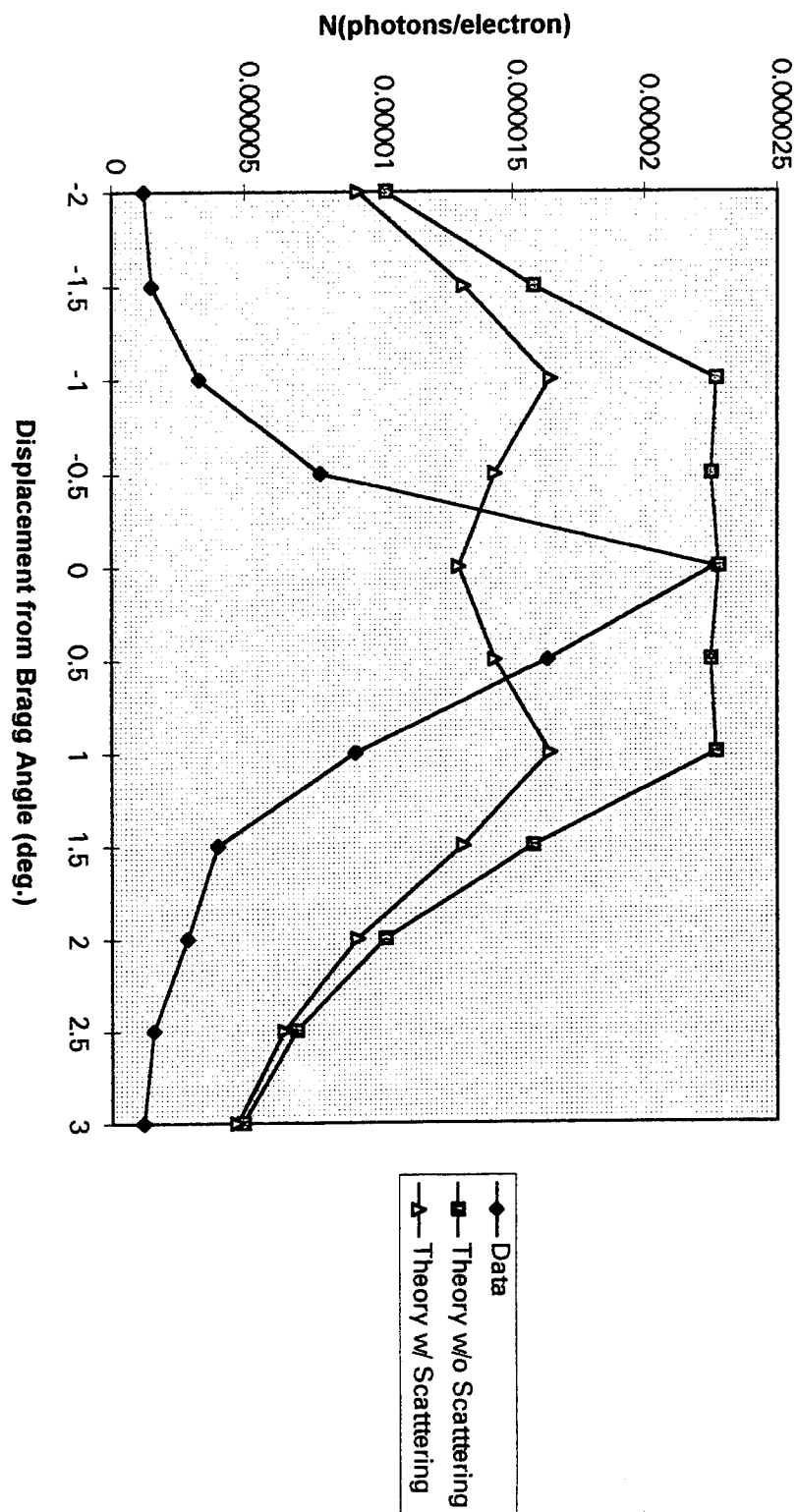


Figure 20. Corrected First Order PXR Intensity Comparison with Theory for 0.45° Mosaic Sample.

# 0.45 DEG. SECOND PEAK DATA VS. THEORY

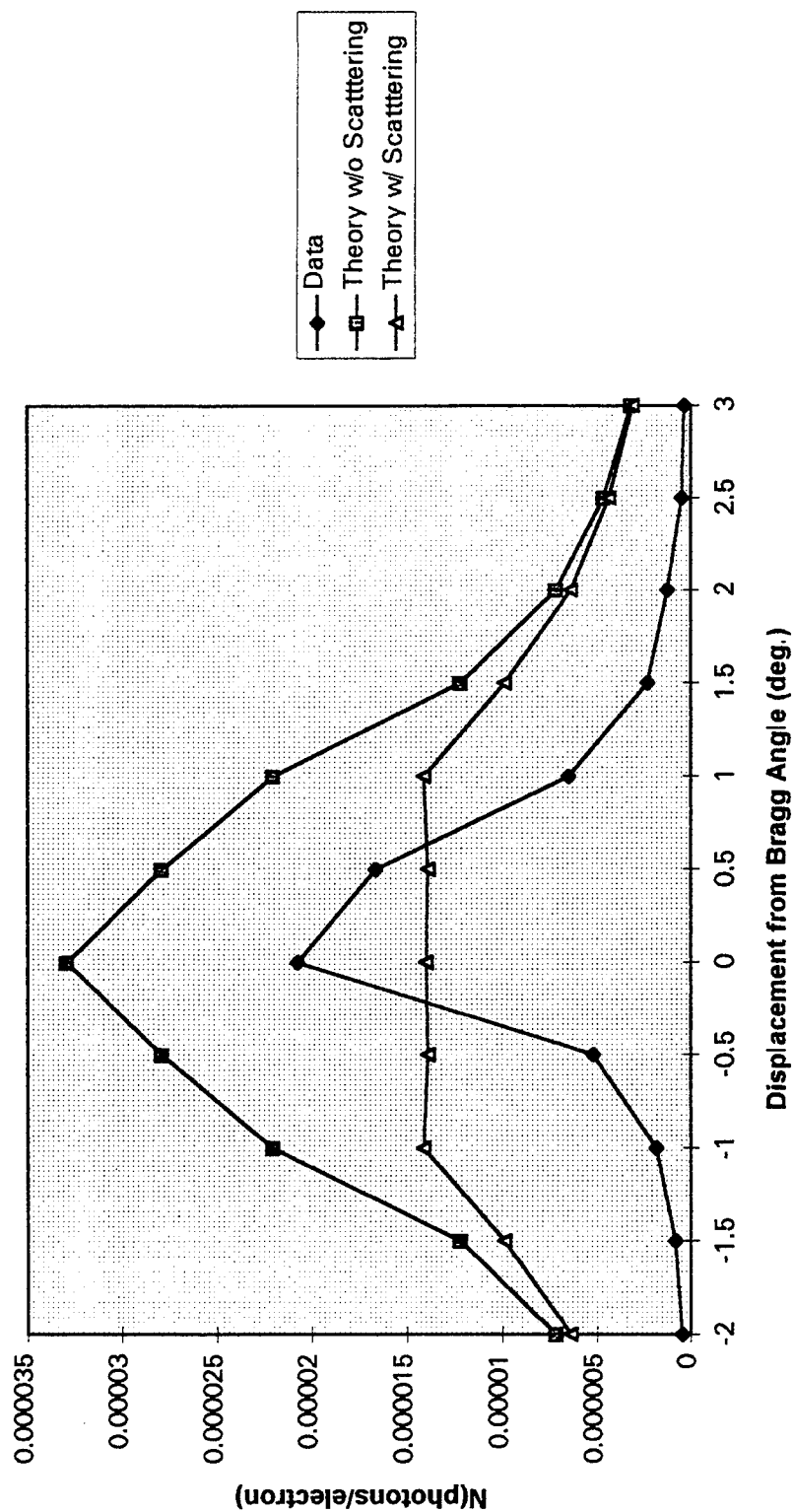


Figure 21. Corrected Second Order PXR Intensity Comparison with Theory for 0.45° Mosaic Sample.

# 1.31 DEG. FIRST PEAK DATA VS. THEORY

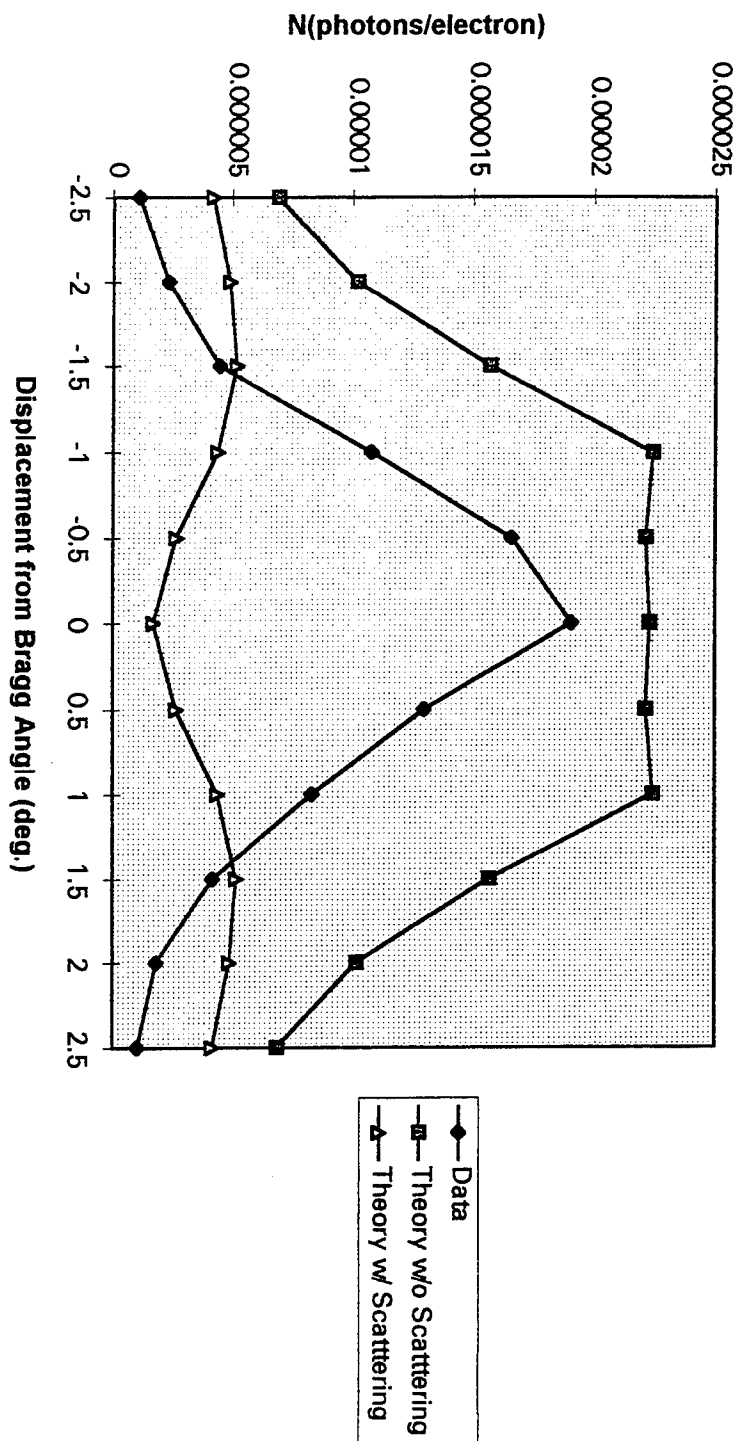


Figure 22. Corrected First Order PXR Intensity Comparison with Theory for 1.31° Mosaic Sample.



# 1.31 DEG. SECOND PEAK DATA VS. THEORY

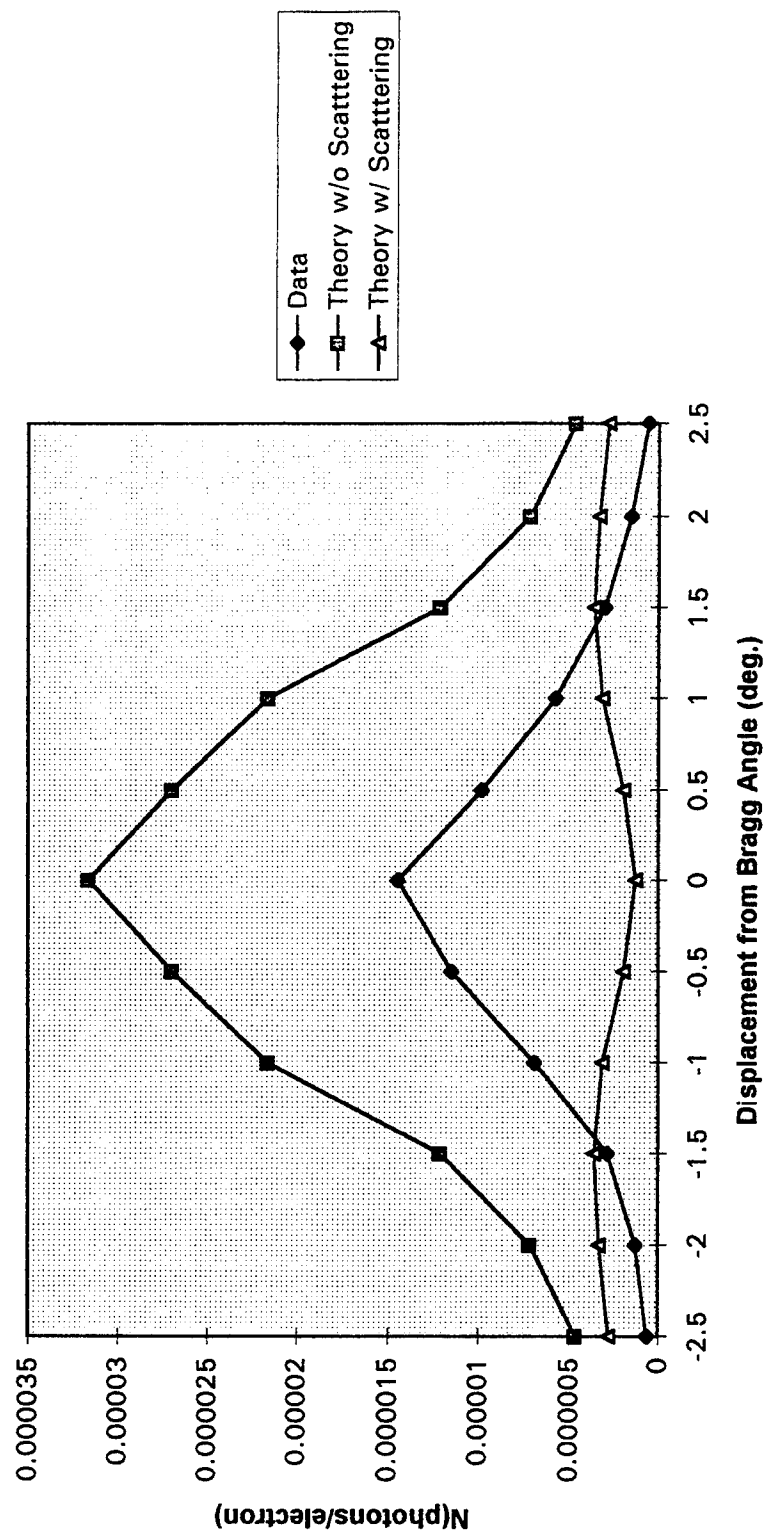


Figure 23. Corrected Second Order PXR Intensity Comparison with Theory for 1.31° Mosaic Sample.

## 2.5 DEG. FIRST PEAK DATA VERSUS THEORY

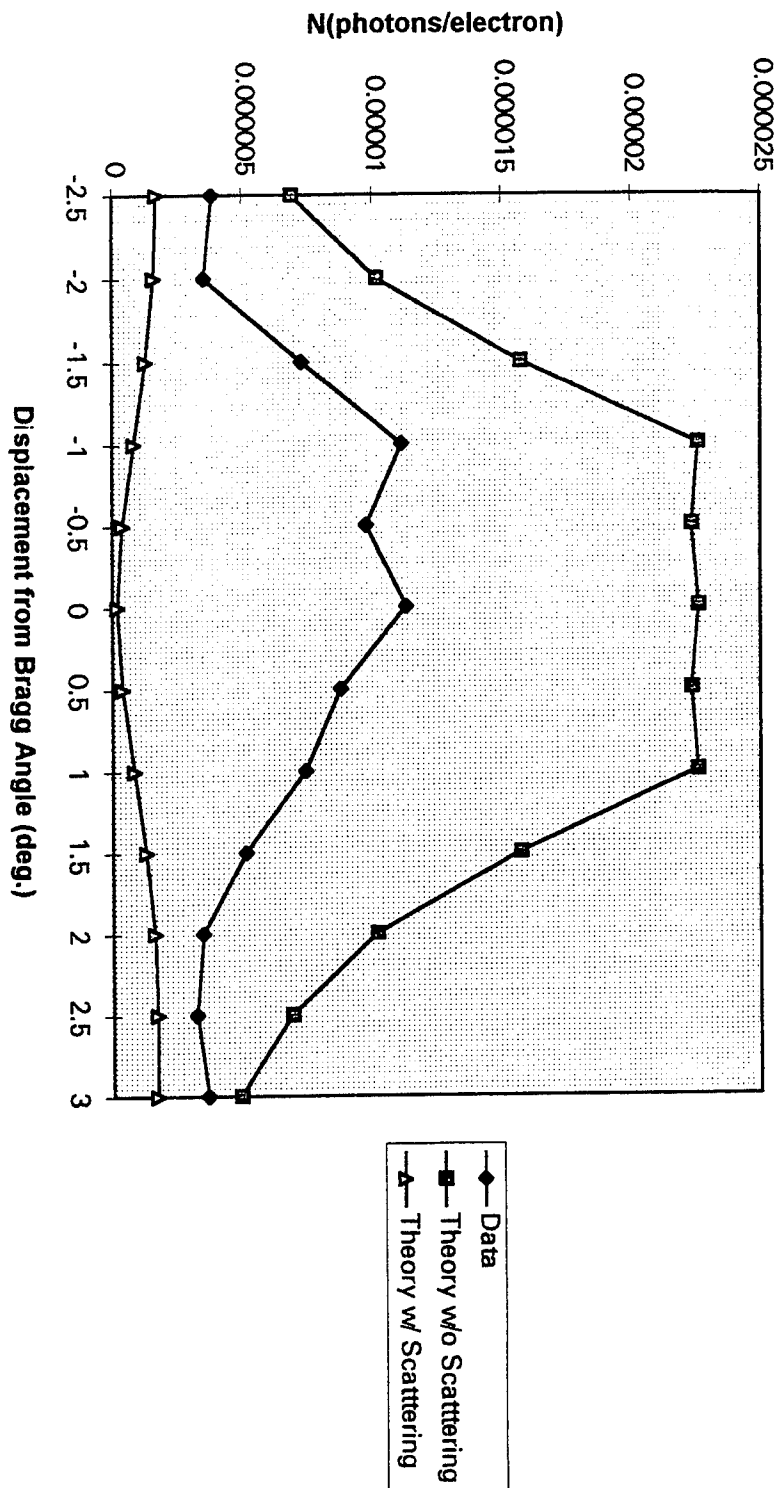


Figure 24. Corrected First Order PXR Intensity Comparison with Theory for 2.5° Mosaic Sample.

# 2.5 DEG. SECOND PEAK DATA VS. THEORY

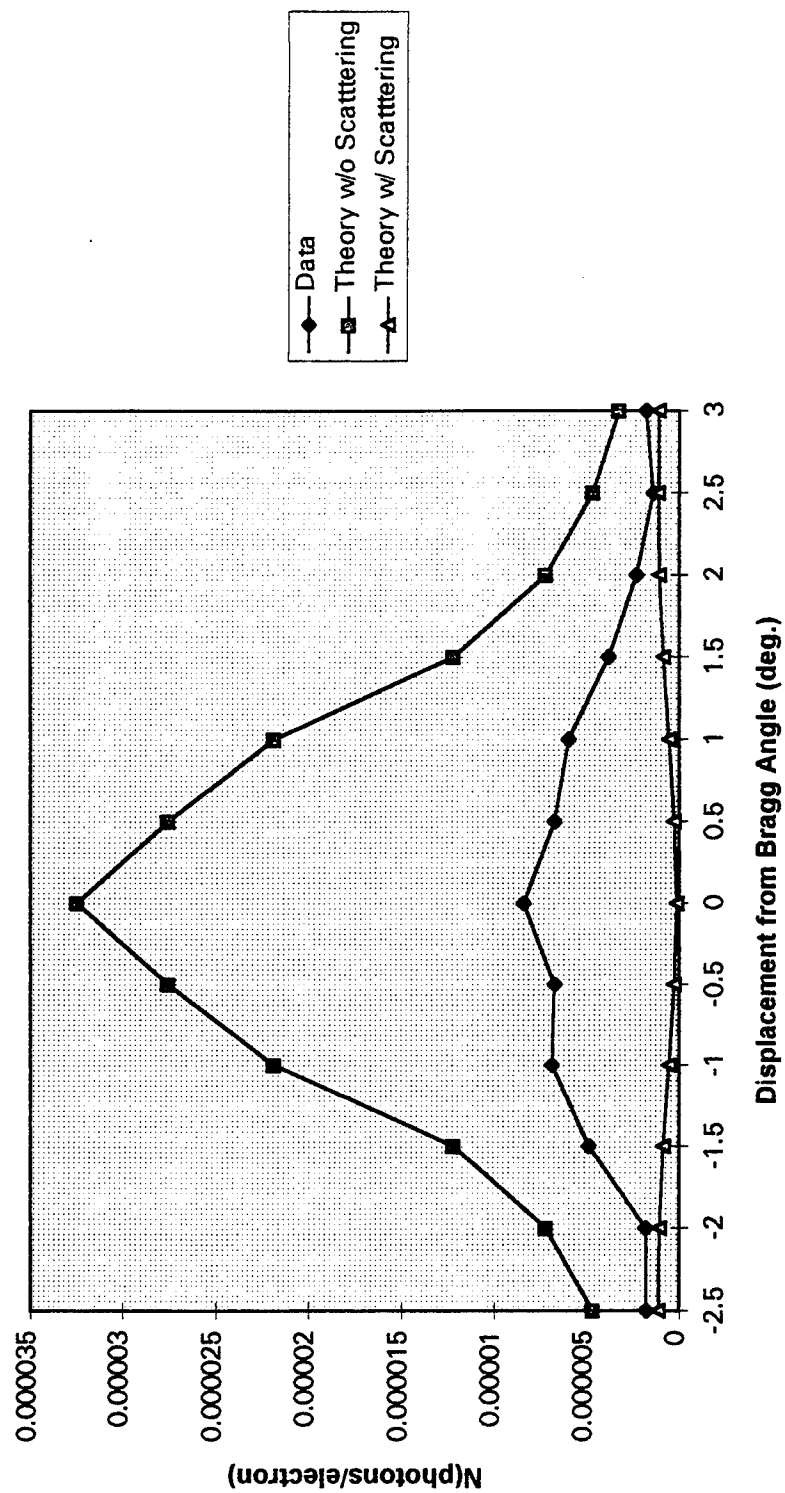


Figure 25. Corrected Second Order PXR Intensity Comparison with Theory for 2.5° Mosaic Sample.

Mosaic Spread	N = 1	N = 2	N(2)/N(1)
0.45°	2.14e-5	7.81e-6	0.36
1.31°	1.63e-5	5.79e-6	0.36
2.5°	1.06e-5	3.70e-6	0.35

Table 5. Theoretical Intensity Comparisons Using Rule et al for Detector Solid Angle of  $4.15\text{e-}4$  sr. [Ref. 19]

#### D. CORRECTIONS TO PREVIOUS DATA

The same  $0.45^\circ$  mosaic spread sample was used in recent experiments as was used in prior experiments. DiNova [Ref 4] measured photon yield (N) with the detector placed at 100 cm and 29 cm from the target which will be referred to as the “far field” and “near field” cases respectively. DiNova calculates the effective thickness of tin used in the absolute yield calculations by dividing the thickness of the tin sample by the cosine of  $\theta_B$ . [Ref. 16] As presented earlier, this should be divided by the sine of  $\theta_B$ . Once this correction is made to DiNova’s data, the comparison between her data, and recent data reveals similar results. Differing detector solid angles account for most of the difference between recent data and the older near and far field data. Other differences include varying tin foil thicknesses, different detectors, and different data analysis procedures. Table 6 summarizes these differences. In order to determine how large the effect of the differing data analysis techniques was, DiNova’s raw data was reprocessed in the exact manner as for the three samples presented here. For comparison purposes, Table 7 shows the first order peak data using the corrected effective tin thickness from DiNova’s thesis and DiNova’s data re-analyzed. Figures 26 and 27 compare this data graphically. An attempt was made to re-analyze the data for the  $25.6^\circ$  spectrum, but the first order peak was not distinguishable. DiNova’s re-analyzed near field and far field and the recent  $0.45^\circ$  mosaic sample data are also compared in Table 8 to show how the distance from detector to target effects the absolute yield. It is important to note that the new data fell at a distance that was in between DiNova’s far and near field results.

	Near Field Data	New Data	Far Field Data
<b>Solid Angle (<math>\Omega</math>)</b>	2.39e-3 sr.	4.15e-4 sr.	2.0e-4 sr.
<b>Tin Thickness (<math>t_L</math>)</b>	$27.5 \pm 1 \mu\text{m}$	$152 \pm 1 \mu\text{m}$	$27.5 \pm 1 \mu\text{m}$
<b>Detector</b>	Canberra Si(Li)	Canberra Si(Li)	ORTEC Si(Li)
<b>Analysis Procedure</b>	Summed Counts in PXR Peak	Peakfit v3.0	Summed Counts in PXR Peak

Table 6. Summary of Differences between Prior and Recent Experiments.

Angle ( $\theta_B$ )	Near Field Data	Near Field Data Re-Analyzed	Far Field Data	Far Field Data Re-Analyzed
20.1°	3.80e-6	3.60e-6	-	-
21.1°	1.36e-5	1.28e-5	2.27e-6	5.12e-7
21.6°	3.01e-5	2.73e-5	5.46e-7	9.30e-7
22.1°	4.70e-5	2.71e-5	1.14e-6	2.55e-6
22.6°	6.22e-5	5.49e-5	4.68e-6	8.49e-6
23.1°	3.82e-5	3.30e-5	3.87e-6	2.07e-6
23.6°	1.58e-5	1.28e-5	8.74e-7	1.59e-6
24.1°	8.07e-6	7.33e-6	4.25e-7	7.75e-7
24.6°	6.47e-6	4.77e-6	3.06e-7	4.59e-7
25.6°	4.76e-6	-	-	-

Table 7. Comparison of DiNova's Data Corrected for the Effective Tin Thickness and DiNova's Data Re-Analyzed Using PeakFit (0.45° Mosaic Spread).

By changing the distance from the target to the detector, the solid angle of the detector is changed. As can be seen in Figure 28 for the three different solid angles, there is a marked effect on the photon yield (N) as the distance is increased.

	Near Field Data	New Data	Far Field Data
<b>Solid Angle (<math>\Omega</math>)</b>	2.39e-3 sr.	4.15e-4 sr.	2.0e-4 sr.
<b>Displ. Angle (<math>\theta</math>)</b>	<b>N(photons/elec.)</b>	<b>N(photons/elec.)</b>	<b>N(photons/elec.)</b>
-2.5°	3.60e-6		
-2.0°		1.21e-6	
-1.5°	1.28e-5	1.50e-6	5.12e-7
-1.0°	2.73e-5	3.29e-6	9.30e-7
-0.5°	2.71e-5	7.81e-6	2.55e-6
0°	5.49e-5	2.27e-5	8.49e-6
0.5°	3.29e-5	1.63e-5	2.07e-6
1.0°	1.28e-5	9.12e-6	1.56e-6
1.5°	7.33e-6	3.99e-6	7.75e-7
2.0°	4.76e-6	2.85e-6	4.59e-7
2.5°		1.56e-6	
3.0°		1.18e-6	

Table 8. Comparison of 0.45° Mosaic Sample Results by Solid Angle.

As can be easily seen from Figures 16 and 17, as the mosaic spread of the crystal increases, the angular distribution of the “rocking curve” also increases. The PeakFit software was again used to obtain the full width at half maximum for the first order peaks. The resulting distribution appears linear and is shown in Figure 29. Thus, increasing crystal mosaicity relaxes the coherence condition and spreads out the resulting “rocking curve” angular distribution.

# NEAR FIELD COMPARISON

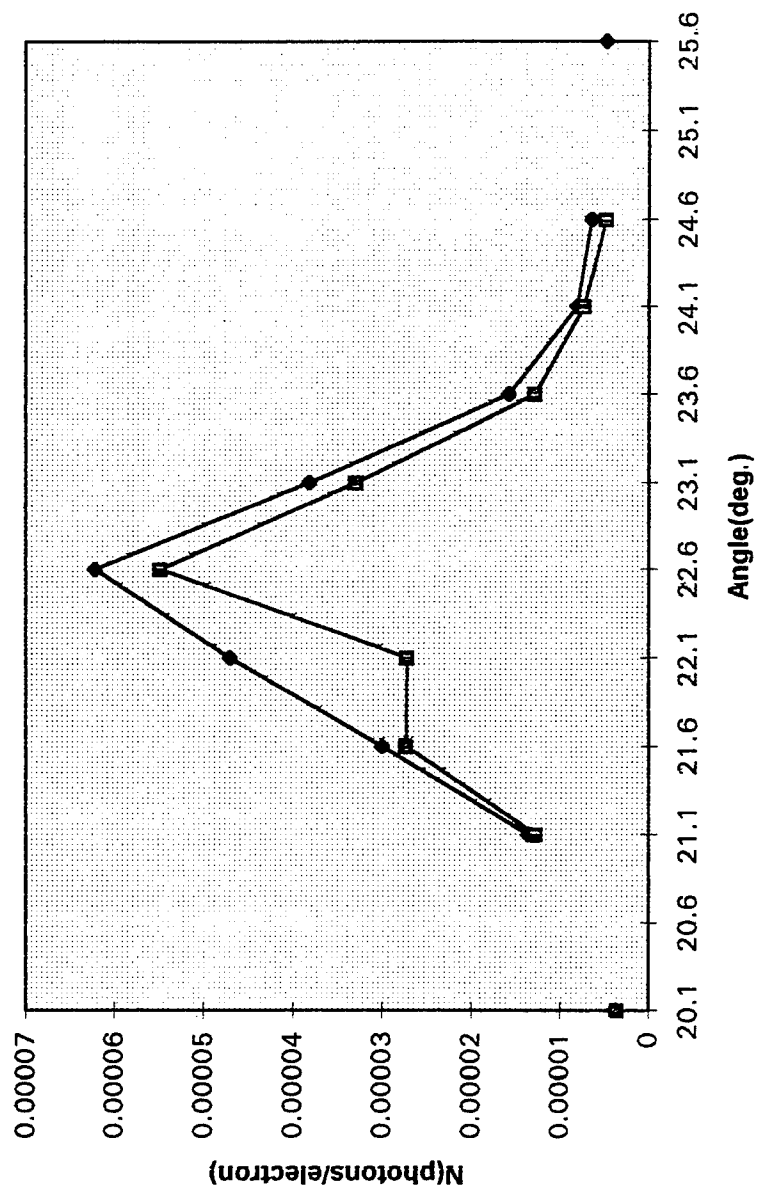


Figure 26. Comparison of Corrected and Re-Analyzed Data for 0.45° Sample for Detector Solid Angle of  $2.39 \times 10^{-3}$  sr.

# FAR FIELD COMPARISON

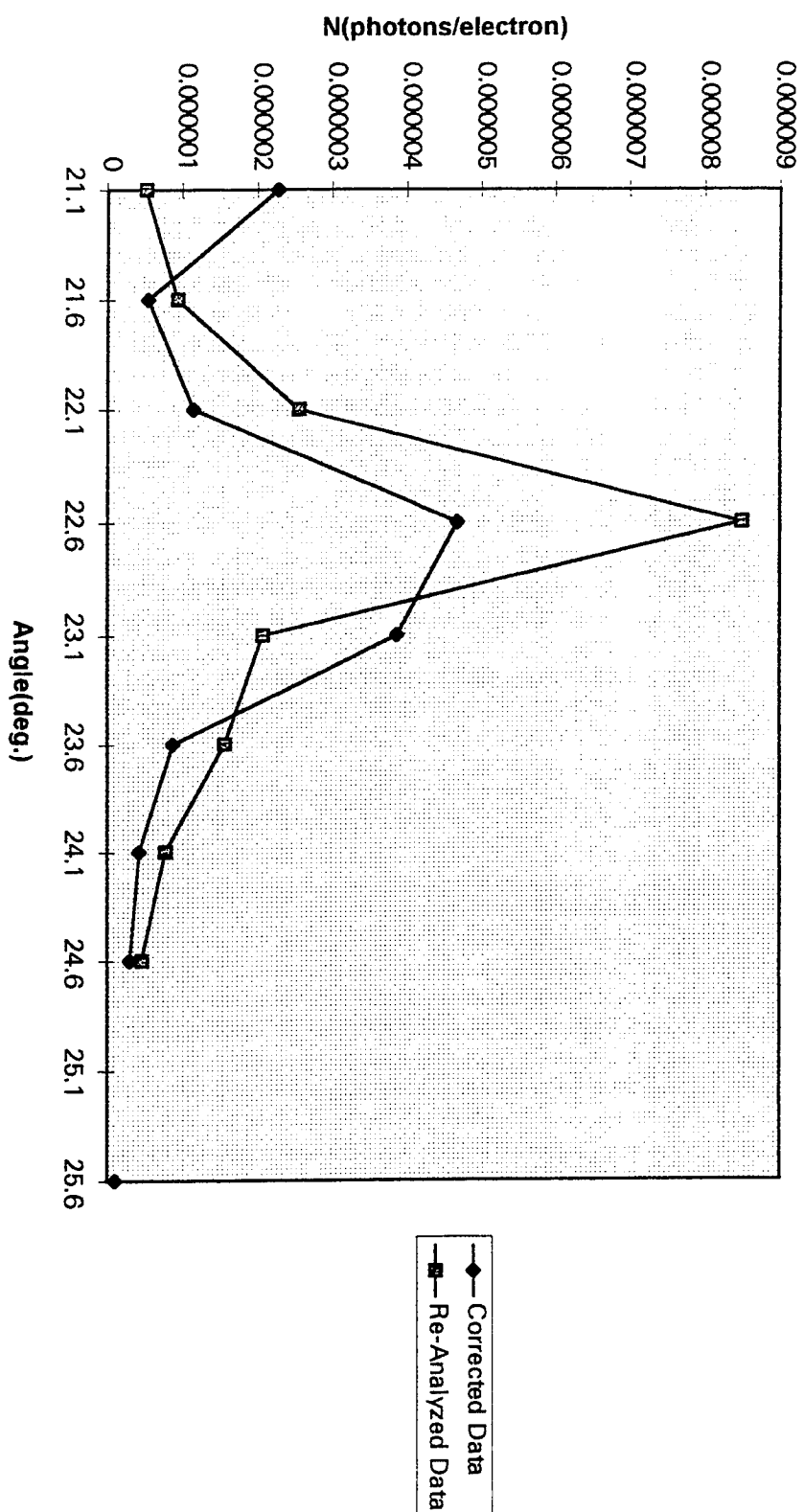


Figure 27. Corrected and Re-Analyzed Data for Far Field 0.45° Mosaic Sample for Detector Solid Angle of 2.0e-4 sr.



# SOLID ANGLE EFFECTS ON PHOTON YIELD

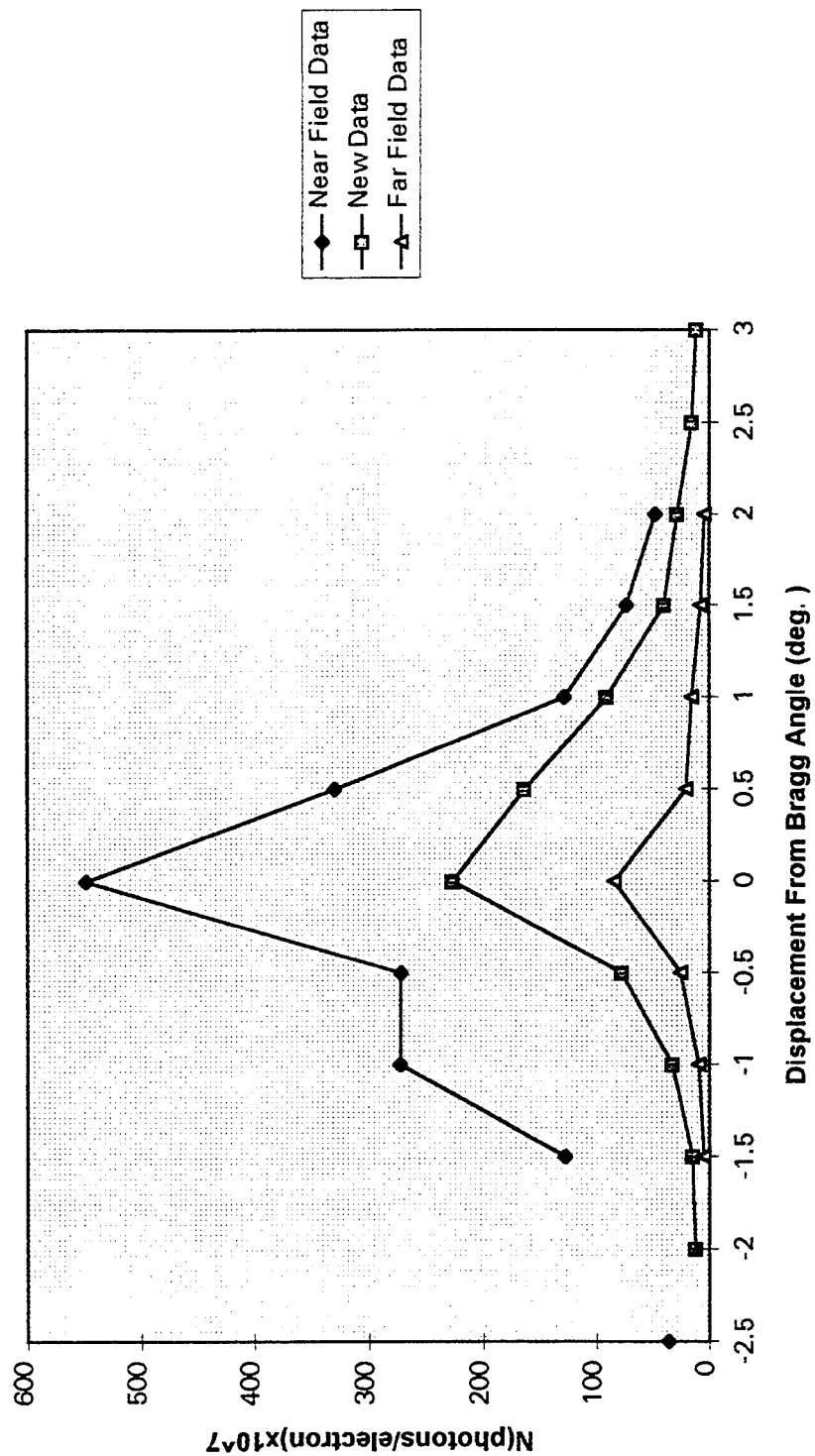


Figure 28 0.45° Mosaic Sample Intensities by Solid Angle.

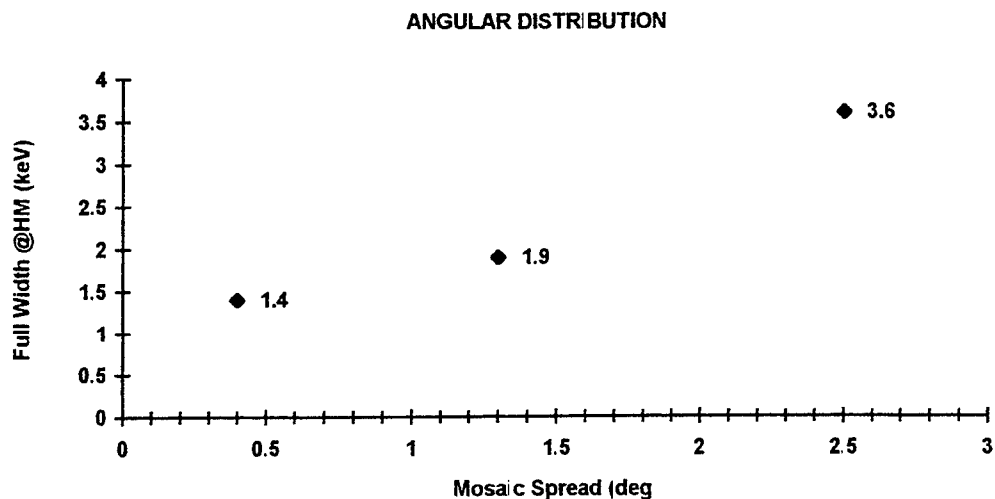


Figure 29. Full Width at Half Maximum of First Order Peaks as a Function of Mosaic Spread.

## E. ERROR ANALYSIS

There are two possible sources of errors in this experiment, namely, systematic and random errors. The sources of systematic errors are caused by limitations of the systems used and effect all measurements in the same fashion. These errors are often hard to analyze and to even detect by statistical analysis. Random errors are experimental uncertainties that can be revealed by doing the same measurements a number of times to get an average value of the measurement. Treatment of the two types of errors are handled differently. [Ref. 20]

In handling systematic errors, the best analysis is to predict the possible sources and verify that these errors will be less than the precision that is required for the experiment. The systematic errors for this experiment are the angle of target incidence which is due to the mechanical motor that turns the target and is subject to over and/or under rotation. The beam alignment is also a systematic error that would not have an effect on each individual run, but when comparing different days runs, this error will be evident. This error also effects the number of electrons that actually strike the target crystal and tin foil which is a value that is calculated from the areas of the spectra. The

combination of these errors produced a shifting of maximum intensities of 0.5° for the 0.45° mosaic sample, and 1.0° for the 1.31° and 2.5° samples. This error is evident when comparing the maximum experimental intensities to the calculated theoretical peak intensities.

The random errors are handled by adding in quadrature the errors involved with the variables used in calculating the number of photons per electron as seen in Equation 16. The only two terms which contribute to this calculation are the areas of the PXR peaks and the area of the tin peak. Equation 20 was used to calculate the fractional error in the number of photons per electron. The random errors in area were analyzed using Equation 21.

$$\frac{\delta N}{N} = \sqrt{\left(\frac{\delta Area_{PXR}}{Area_{PXR}}\right)^2 + \left(\frac{\delta Area_{Tin}}{Area_{Tin}}\right)^2} \quad (20)$$

$$\frac{\delta F}{F} = \int_{-\infty}^{\infty} \frac{e^{-\left(\frac{x-a_1}{a_2}\right)^2} \cdot (x-a_1) \cdot \frac{da_1}{(a_2)^2} + e^{-\left(\frac{x-a_1}{a_2}\right)^2} \cdot (x-a_1)^2 \cdot \frac{da_2}{(a_2)^3}}{F} \cdot dx + \frac{da_0}{a_0} \quad (21)$$

where F is the counts in a spectral peak,  $a_0$  is the height of the PXR peak,  $a_1$  is the center channel of the PXR peak,  $a_2$  is the standard deviation of the curve fitted peak used by Peakfit to determine the best fit peak, and  $da_0$ ,  $da_1$ , and  $da_2$  are the errors in each of these values respectively that are provided by the Peakfit Peak Analysis Program. The integral was processed using a MathCad [Ref. 18] program that is listed in Appendix B for each peak of the PXR spectrum and the tin peak for each spectrum. The errors in the PXR peak and the tin peak are then added in quadrature to obtain the total error for each calculation of the number of photons per electron. Table 9 lists the results of Equations 20 and 21 as well as those from adding in quadrature the errors in the  $Area_{PXR}$  and  $Area_{Tin}$  using Equation 22 for each of the first peaks for each spectra. Figures 30 through 34

$$\frac{\delta N}{N} = \sqrt{\left(\frac{\sqrt{Area_{PXR}}}{Area_{PXR}}\right)^2 + \left(\frac{\sqrt{Area_{Tin}}}{Area_{Tin}}\right)^2} \quad (22)$$

Angle( $\theta_B$ )	0.45° Mosaicity		1.31° Mosaicity		2.5° Mosaicity	
	MCAD	1/ $\sqrt{\text{Area}}$	MCAD	1/ $\sqrt{\text{Area}}$	MCAD	1/ $\sqrt{\text{Area}}$
21.0°	.0079	.062	.0078	.054	.0164	.042
21.5°	.0082	.064	.0091	.036	.0192	.042
22.0°	.0113	.041	.0107	.019	.0247	.027
22.5°	.0262	.026	.0252	.012	.0515	.028
23.0°	.1747	.018	.0499	.010	.0405	.023
23.5°	.0805	.018	.0782	.014	.0411	.023
24.0°	.0303	.023	.0420	.015	.0345	.022
24.5°	.0131	.035	.0131	.027	.0276	.027
25.0°	.0094	.035	.0174	.036	.0214	.033
25.5°	.0070	.052	.0089	.057	.0149	.037
26.0°	.0061	.059	.0069	.062	.0154	.039

Table 9. Estimation of the Random Error in PXR Intensity (N) Calculation Using Equations 20, 21, and 22.

show the random error based on Equations 20 and 21 in the earlier near and far field re-analyzed 0.45° mosaic spread data as well as the new data for each of the first order peaks. Using this method, larger intensity peaks incurred a larger fractional error due to the relatively larger size of the peak.

# 0.45 DEG. NEAR FIELD ERROR

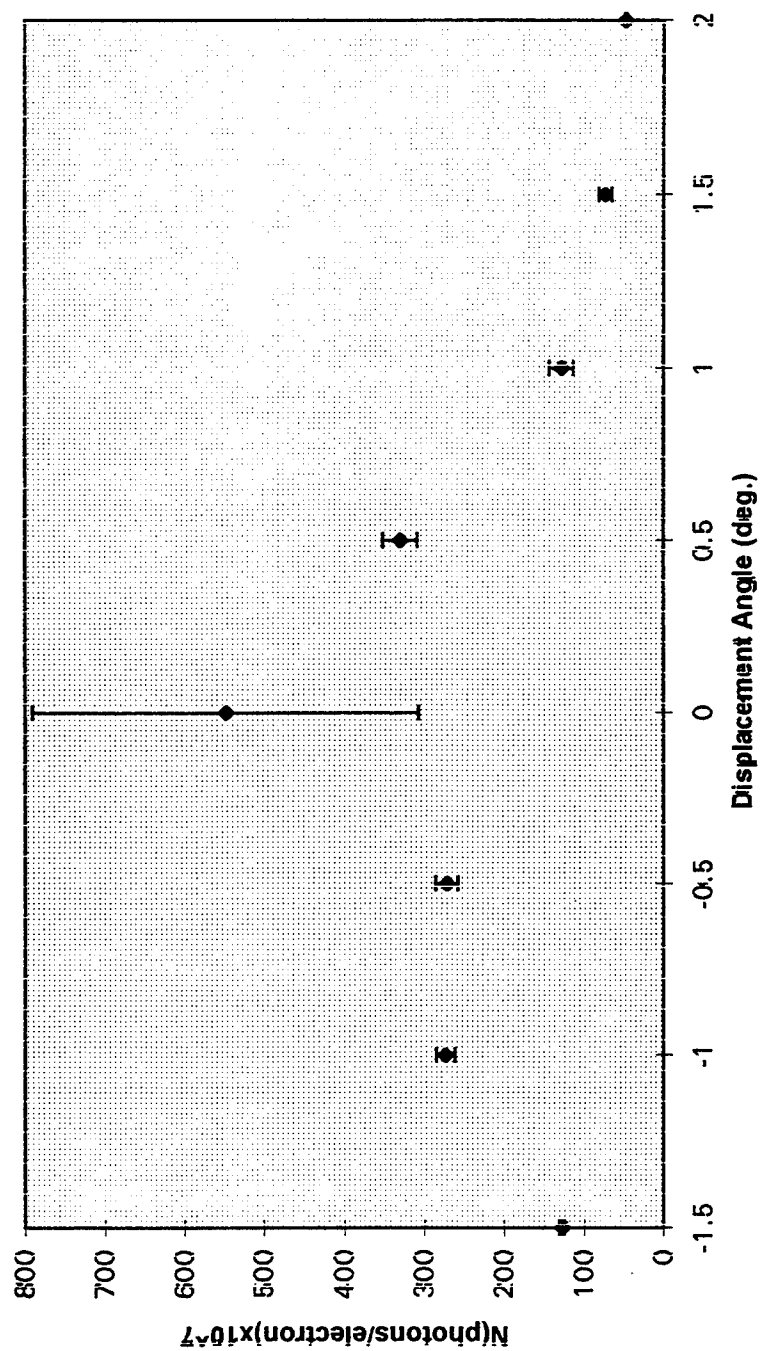


Figure 30. Random Error Distribution for 0.45° Mosaic Sample With Detector Solid Angle of  $2.39 \times 10^{-3}$  sr.

# 0.45 DEG. FAR FIELD ERROR

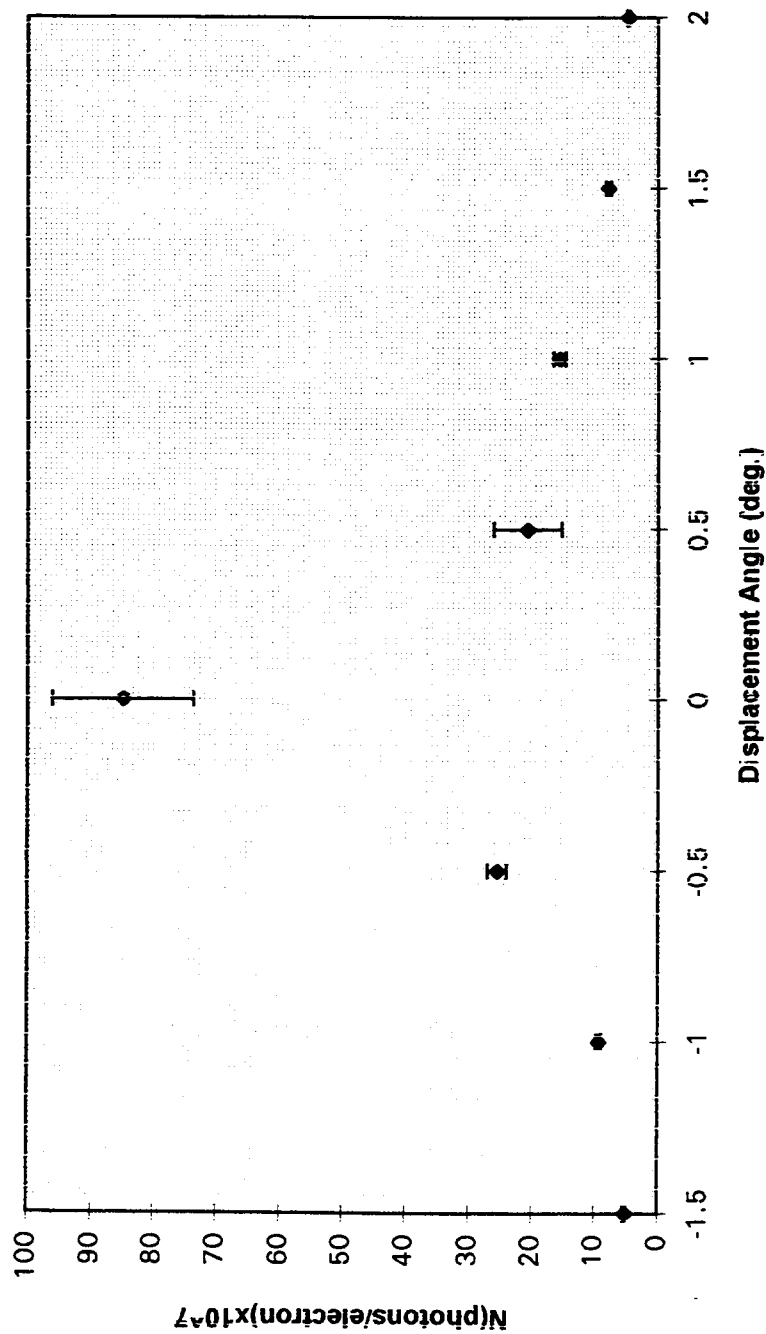


Figure 31. Random Error Distribution for 0.45° Mosaic Sample With Detector Solid Angle of  $2.0 \times 10^{-4}$  sr.

# 0.45 DEGREE MOSAICITY

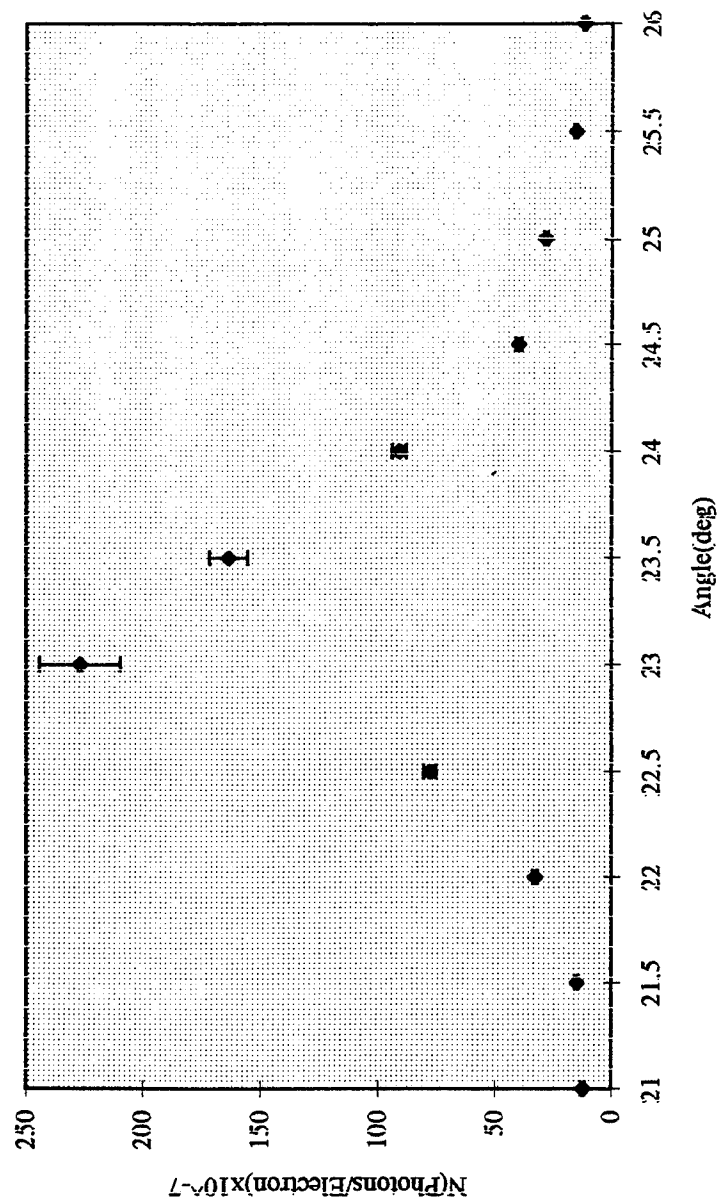


Figure 32. Random Error Distribution for 0.45° Mosaic Sample With Detector Solid Angle of  $4.15 \times 10^{-4}$  sr.

# 1.31 DEGREE MOSAICITY

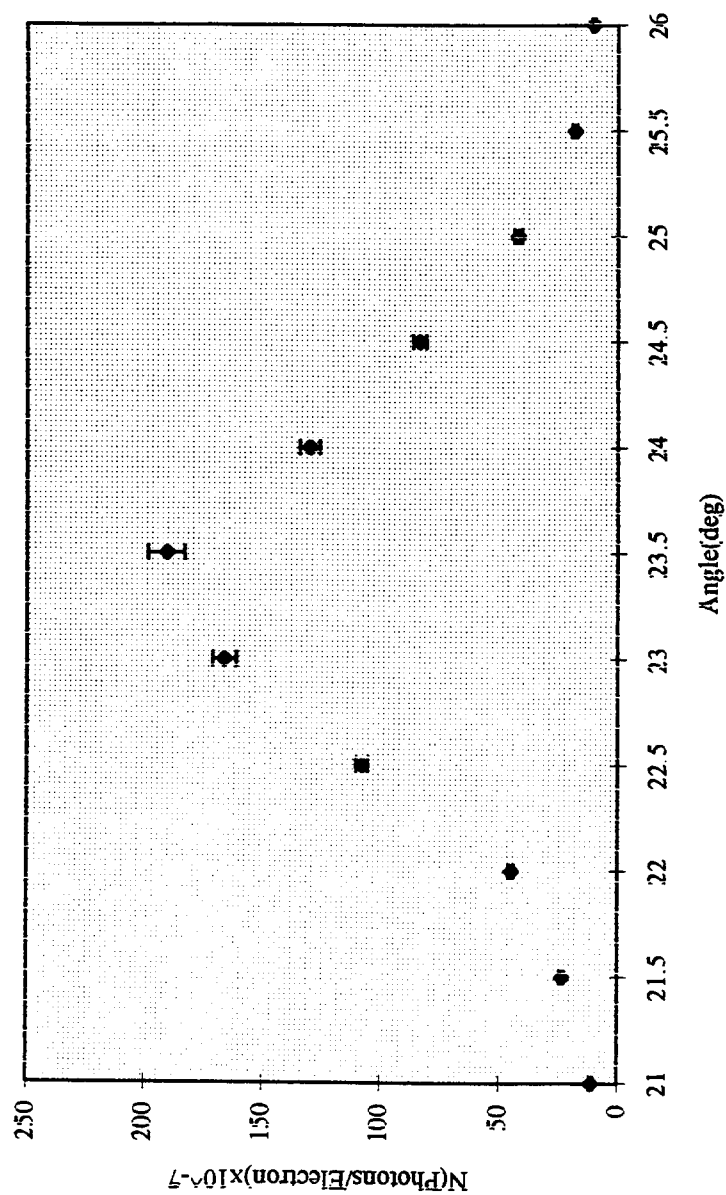


Figure 33. Random Error Distribution for 1.31° Mosaic Sample With Detector Solid Angle of  $4.15 \times 10^{-4}$  sr.



## 2.5 DEGREE MOSAICITY

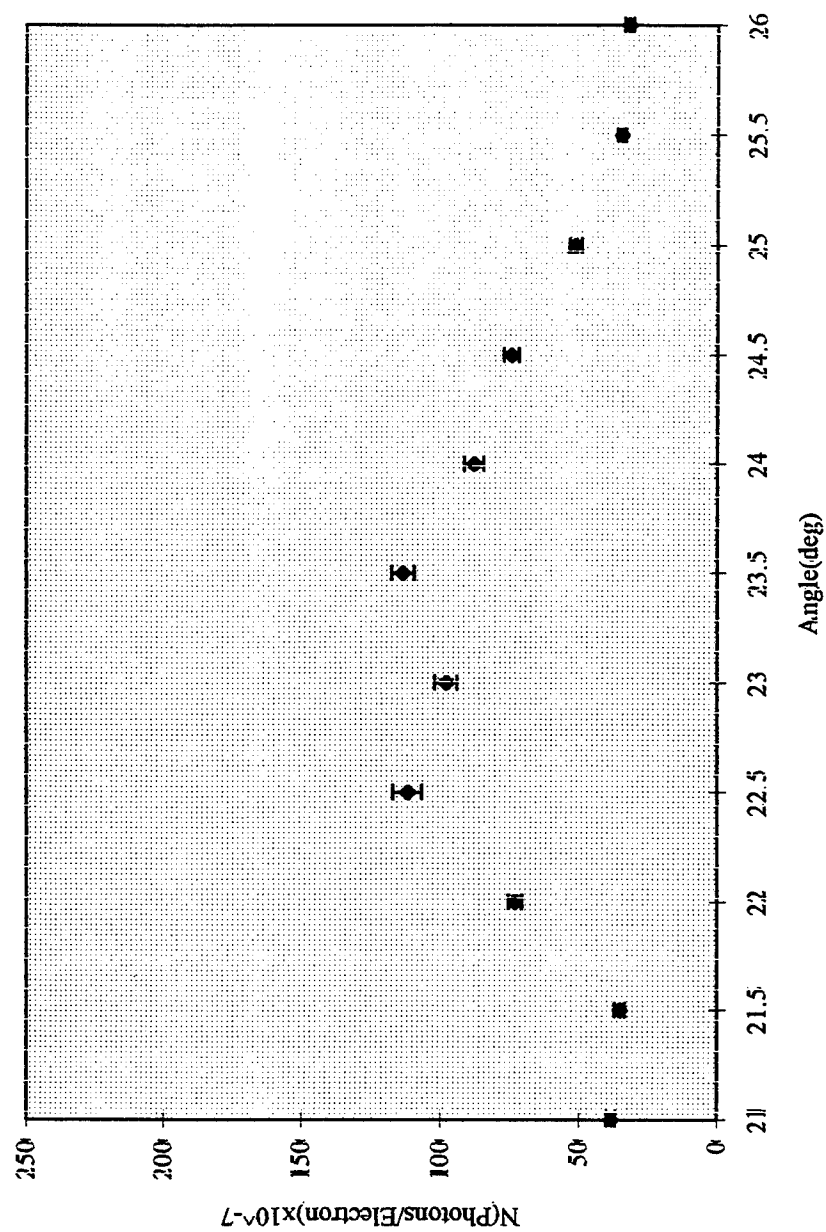


Figure 34. Random Error Distribution for 2.5° Mosaicity Sample With Detector Solid Angle of  $4.15 \times 10^{-4}$  sr.



## V. CONCLUSIONS AND RECOMMENDATIONS

As suspected from previous experimental and theoretical comparisons, the mosaic spread of the crystal used does have a definite effect on the outcome of the PXR spectra and the resulting intensities and absolute yields. Much work is being done by Rule et al to model theoretically the effect of the mosaic spread on PXR scattering. The theory presented by Rule et al [Ref. 5] seems to predict within experimental errors the data obtained through the use of the three samples for this thesis more than the older theories that were previously used. The work of Rule et al incorporates the mosaic spread, which the previous work by Feranchuck and Ivansin [Ref. 6] neglected. As can be seen by Figures 16, 17, and 29 an increase in the mosaic spread relaxes the coherence condition and spreads out the angular distribution of the scattered photons. Previous data used a miscalculated effective thickness for the tin which made the absolute calculated yield appear higher than it should have been. In the same comparison, the theory was also miscalculated making it to appear lower. By correcting for these two mistakes, the data and the theory are more comparable, but there still needs to be the correction for the mosaic spread as it does have an effect. Theoretical calculations need to be done to support the off Bragg condition measurements as well as the higher order peak yields from theory presented by Rule et al. Through more experimental data and more theoretical calculations to compare with, a better understanding of the mosaic effects on PXR spectra can be achieved.

Future thesis topics should investigate the same samples in a "far field" configuration as well as new samples with different mosaic spreads. Contacts should be maintained with Rule et al to continue to compare past and present data with new theoretical calculations as they become available.



## APPENDIX A. SAMPLE THEORETICAL YIELD PROGRAM

Parametric x-ray generation (Q.Li 5/26/92 carbon3.mcd)

Differential cross section calculation

Carbon (002)

Input parameters:

$\theta_B := 22.5$	degree	$\theta_A := 0.45$	degree
$d := 6.7078$	Angstrom	$L := 1659$	$\mu\text{m}$
$m_a := 12.011$	gm molar mass	$\rho_a := 2.26$	gm/cc density
$V := 35.189$	cubic angstrom	$E_e := 95.32$	MeV
$Z_a := 6$	Atomic number	$\theta_{\text{mos}} := \frac{1.31 \cdot \pi}{180}$	

Constants

$e_c := 1.6021917 \cdot 10^{-19}$	Electron charge
$m := 9.109558 \cdot 10^{-31}$	Electron mass
$c := 299792458$	speed of light
$\alpha := 7.297351 \cdot 10^{-3}$	Fine structure constant
$\hbar := \frac{6.626196 \cdot 10^{-34}}{(2 \cdot \pi)}$	Plank's constant
$N_A := 6.022169 \cdot 10^{23}$	Avogadro constant
$r_e := 2.817938 \cdot 10^{-15}$	Classical electron radius

Unit conversion

$$\theta_B := \pi \cdot \frac{\theta_B}{180} \quad \theta_\Delta := \pi \cdot \frac{\theta_\Delta}{180}$$

$$L := \frac{L \cdot 10^{-6}}{\sin(\theta_B)} \quad V := V \cdot 10^{-30} \quad \rho_\alpha := \rho_\alpha \cdot 10^6 \quad d := d \cdot 10^{-10}$$

Bragg frequency calculation

i := 4      Order of Bragg reflection

$$\omega_B := \frac{i \cdot \pi \cdot c}{d \cdot \sin(\theta_B)} \quad \text{Bragg frequency function}$$

Absorption length calculation

Absptn := READPRN(carbon)

Input is associated with absorption data file \*.prn generated by xcom.exe in units of MeV vs barns

i := 0..rows(Absptn) - 1

Absptn<sub>i,0</sub> := log(Absptn<sub>i,0</sub>) + 6

Absptn<sub>i,1</sub> := log(Absptn<sub>i,1</sub>) - 28

$$L_a(\omega) := \frac{m_a}{N_A \cdot \rho_\alpha} \cdot 10^{-\text{interp}\left(\text{Absptn}^{<0>}, \text{Absptn}^{<1>}, \log\left(\frac{\omega \cdot h \text{ bar}}{e_c}\right)\right)}$$

Atomic form factor function

cf. International Tables for x-ray crystallography, Vol. IV 1974 p71

a<sub>1</sub> := 2.31      a<sub>2</sub> := 1.02      a<sub>3</sub> := 1.5886      a<sub>4</sub> := 0.865

b<sub>1</sub> := 20.8439      b<sub>2</sub> := 10.2075      b<sub>3</sub> := 0.5687      b<sub>4</sub> := 51.6512

c<sub>0</sub> := 0.2156

i := 1..4

Input parameters

$$f(x) := \sum_i a_i \cdot \exp\left[-b_i \cdot (x \cdot 10^{-10})^2\right] + c_0$$

x should be sin(θ)/λ

Dielectric function

$$\Gamma_{\omega}(\omega) := \frac{r_e \cdot (2 \cdot \pi \cdot c)^2}{\pi \cdot V \cdot \omega^2}$$

$$x(\omega) := \frac{\sin(\theta_B)}{2 \cdot \pi \cdot c} \cdot \omega$$

$$S_f := 16$$

Input parameter: Selection factor

$$\chi_{10}(\omega) := \Gamma_{\omega}(\omega) \cdot f(x(\omega)) \cdot \sqrt{S_f}$$

$$\chi_0(\omega) := \frac{1}{2} \cdot (28.816^2) \cdot \frac{(\rho_{\alpha}) \cdot 10^{-6}}{\left[ m_a \cdot \left( \omega \cdot \frac{h_{\text{bar}}}{e_c} \right)^2 \right]} \cdot f(x(\omega))$$

N calculation

$$\frac{\omega_B \cdot h_{\text{bar}}}{e_c \cdot 1000} =$$

keV

$$\rho_s = \frac{c}{\omega_B \cdot L_a(\omega_B)} =$$

$$L_a(\omega_B) \cdot 10^6 =$$

μm

$$N_b(\theta_{\xi}, \theta_{\psi}) := \frac{\alpha \cdot \omega_B \cdot (|\chi_{10}(\omega_B)|)^2 \cdot L_a(\omega_B)}{\pi \cdot 4 \cdot \sin(\theta_B)^2 \cdot c} \cdot \frac{\left[ \theta_{\xi}^2 \cdot (\cos(2 \cdot \theta_B))^2 + \theta_{\psi}^2 \right]}{\left[ \left( \frac{0.511}{E_e} \right)^2 + \theta_{\xi}^2 + \theta_{\psi}^2 + |\chi_0(\omega_B)| \right]^2}$$

$$\delta\theta_1 := 0.011522$$

$$\delta\theta_\Delta := 0.03 \cdot \tan(\theta_B)$$

$$\delta\theta_\Delta =$$

$$\delta\theta_2 := 0.011522$$

$$\frac{0.511}{E_e} =$$

$$i := 1..8$$

$$\theta := 0$$

$$z_1 := \int_{\theta - \delta\theta_1}^{\theta + \delta\theta_1} \int_{-\delta\theta_2}^{\delta\theta_2} N_b(\theta_\xi, \theta_\psi) d\theta_\xi d\theta_\psi$$

$$\theta := .008727$$

$$z_2 := \int_{\theta - \delta\theta_1}^{\theta + \delta\theta_1} \int_{-\delta\theta_2}^{\delta\theta_2} N_b(\theta_\xi, \theta_\psi) d\theta_\xi d\theta_\psi$$

$$\theta := .017453$$

$$z_3 := \int_{\theta - \delta\theta_1}^{\theta + \delta\theta_1} \int_{-\delta\theta_2}^{\delta\theta_2} N_b(\theta_\xi, \theta_\psi) d\theta_\xi d\theta_\psi$$

$$\theta := .02618$$

$$z_4 := \int_{\theta - \delta\theta_1}^{\theta + \delta\theta_1} \int_{-\delta\theta_2}^{\delta\theta_2} N_b(\theta_\xi, \theta_\psi) d\theta_\xi d\theta_\psi$$

$$\theta := .034907$$

$$z_5 := \int_{\theta - \delta\theta_1}^{\theta + \delta\theta_1} \int_{-\delta\theta_2}^{\delta\theta_2} N_b(\theta_\xi, \theta_\psi) d\theta_\xi d\theta_\psi$$

$$\theta := .043633$$

$$z_6 := \int_{\theta - \delta\theta_1}^{\theta + \delta\theta_1} \int_{-\delta\theta_2}^{\delta\theta_2} N_b(\theta_\xi, \theta_\psi) d\theta_\xi d\theta_\psi$$

$$\theta := .05236$$

$$z_7 := \int_{\theta - \delta\theta_1}^{\theta + \delta\theta_1} \int_{-\delta\theta_2}^{\delta\theta_2} N_b(\theta_\xi, \theta_\psi) d\theta_\xi d\theta_\psi$$

$$\theta := .061087$$

$$z_8 := \int_{\theta - \delta\theta_1}^{\theta + \delta\theta_1} \int_{-\delta\theta_2}^{\delta\theta_2} N_b(\theta_\xi, \theta_\psi) d\theta_\xi d\theta_\psi$$



$$\theta_{\text{msqr}} := \frac{0.157 \cdot Z_a \cdot (Z_a + 1) \cdot .511^2 \cdot L}{m_a \cdot (E_e)^2} \cdot \log \left[ \frac{1.13 \cdot 10^4 \cdot (Z_a)^{\left(\frac{4}{3}\right)} \cdot .511^2 \cdot L}{m_a} \right]$$

$$N_{b1}(\theta_\xi, \theta_\psi) := \frac{\alpha \cdot \omega_B \left( \left| \chi_{10}(\omega_B) \right| \right)^2 L_a(\omega_B)}{\pi \cdot 4 \cdot \sin(\theta_B)^2} \cdot \frac{\left[ \theta_\xi^2 \cdot (\cos(2 \cdot \theta_B))^2 + \theta_\psi^2 \right]}{\left[ \left( \frac{0.511}{E_e} \right)^2 + \theta_\xi^2 + \theta_\psi^2 + \theta_{\text{msqr}} + (\theta_{\text{mos}})^2 + \left| \chi_{10}(\omega_B) \right| \right]^2}$$

i := 1..8

$$\theta := 0 \quad zz_1 := \int_{\theta - \delta\theta_1}^{\theta + \delta\theta_1} \int_{-\delta\theta_2}^{\delta\theta_2} N_{b1}(\theta_\xi, \theta_\psi) d\theta_\xi d\theta_\psi$$

$$\theta := .008727 \quad zz_2 := \int_{\theta - \delta\theta_1}^{\theta + \delta\theta_1} \int_{-\delta\theta_2}^{\delta\theta_2} N_{b1}(\theta_\xi, \theta_\psi) d\theta_\xi d\theta_\psi$$

$$\theta := .017453 \quad zz_3 := \int_{\theta - \delta\theta_1}^{\theta + \delta\theta_1} \int_{-\delta\theta_2}^{\delta\theta_2} N_{b1}(\theta_\xi, \theta_\psi) d\theta_\xi d\theta_\psi$$

$$\theta := .02618 \quad zz_4 := \int_{\theta - \delta\theta_1}^{\theta + \delta\theta_1} \int_{-\delta\theta_2}^{\delta\theta_2} N_{b1}(\theta_\xi, \theta_\psi) d\theta_\xi d\theta_\psi$$

$$\theta := .034907 \quad zz_5 := \int_{\theta - \delta\theta_1}^{\theta + \delta\theta_1} \int_{-\delta\theta_2}^{\delta\theta_2} N_{b1}(\theta_\xi, \theta_\psi) d\theta_\xi d\theta_\psi$$

$$\theta := .043633 \quad zz_6 := \int_{\theta - \delta\theta_1}^{\theta + \delta\theta_1} \int_{-\delta\theta_2}^{\delta\theta_2} N_{b1}(\theta_\xi, \theta_\psi) d\theta_\xi d\theta_\psi$$

$$\theta := .05236 \quad zz_7 := \int_{\theta - \delta\theta_1}^{\theta + \delta\theta_1} \int_{-\delta\theta_2}^{\delta\theta_2} N_{bl}(\theta_\xi, \theta_\psi) d\theta_\xi d\theta_\psi$$

$$\theta := .061087 \quad zz_8 := \int_{\theta - \delta\theta_1}^{\theta + \delta\theta_1} \int_{-\delta\theta_2}^{\delta\theta_2} N_{bl}(\theta_\xi, \theta_\psi) d\theta_\xi d\theta_\psi$$

$$i := 4 \quad \theta_{\text{mos}} := \frac{1.31 \cdot \pi}{180} \quad \delta\theta_1 := 0.011522$$

$$E_e := 95.32$$

$$L := 1659$$

$$z = \quad zz =$$

z is w/o scattering, zz is with scattering

## APPENDIX B. SAMPLE ERROR ANALYSIS PROGRAM

inputs for peak height:      F is the area under the PXR peak  
 $a_0 := 349.6233$        $da_0 := 3.7878$        $F := 1500.9662$

inputs for peak center channel:

$a_1 := 37.46832$        $da_1 := .021196$

inputs for peak width:

$a_2 := 1.712699$        $da_2 := .02188$

$$\int_0^{80} \frac{e^{-\left(\frac{x-a_1}{a_2}\right)^2} \cdot (x-a_1) \cdot \frac{da_1}{(a_2)^2} + e^{-\left(\frac{x-a_1}{a_2}\right)^2} \cdot (x-a_1)^2 \cdot \frac{da_2}{(a_2)^3}}{F} dx + \frac{da_0}{a_0} = 0.0108$$



## **APPENDIX C. DATA VERSUS THEORY FOR ALL SAMPLES**

This appendix provides a complete comparison of the actual and theoretical intensity ratios between PXR peaks. Theoretical calculations without scattering are based on the integration of Equation 3. Theoretical calculations with scattering account for multiple scattering and mosaic spread based on the integration of Equation 17. Here we also provide a comparison of the observed intensities versus the theoretical intensities both with and without accounting for multiple scattering and mosaic spread as calculated using the MathCad program found in Appendix A.

0.45 DEG. MOSAIC SPREAD DATA											
ANGLE	PEAK #	DATA photons/electron	THEORY w/ scattering	THEORY w/o scattering	DATA N(n)/N(1)	THEORY w/ Scattering N(n)/N(1)	THEORY w/o scattering N(n)/N(1)	DATA w/ scattering	DATA w/o scattering	VS. THEORY w/ scattering	VS. THEORY w/o scattering
neg 2.0 deg from Bragg condition	1	1.21E-06	9.18E-06	1.02E-05	1	1	1	0.1318082	0.11862745		
	2	4.62E-07	6.44E-06	7.22E-06	0.38182	0.70152	0.707843	0.0717391	0.06398892		
	3		3.77E-06	4.23E-06		0.41067	0.414705				
	4		2.24E-06	2.51E-06		0.24400	0.246078				
neg 1.5 deg from Bragg condition	1	1.50E-06	1.31E-05	1.58E-05	1	1	1	0.1145038	0.09493670		
	2	8.27E-07	9.91E-06	1.22E-05	0.55133	0.75648	0.772151	0.0834510	0.06778688		
	3		5.88E-06	7.30E-06			0.4620253				
	4		3.51E-06	4.36E-06		0.26793	0.2759494				
neg 1.0 deg from Bragg condition	1	3.29E-06	1.64E-05	2.27E-05	1	1	1	0.2006097	0.14493392		
	2	1.87E-06	1.41E-05	2.20E-05	0.56839	0.85975	0.969163	0.1326241	0.085		
	3	6.10E-07	8.63E-06	1.39E-05	0.18541	0.52621	0.6123348	0.0706836	0.04388489		
	4		5.19E-06	8.44E-06		0.31646	0.3718062				
neg 0.5 deg from Bragg condition	1	7.81E-06	1.43E-05	2.25E-05	1	1	1	0.5461538	0.34711111		
	2	5.22E-06	1.39E-05	2.79E-05	0.66837	0.97202	1.24	0.3755395	0.18709677		
	3	1.99E-06	8.73E-06	1.90E-05	0.2548	0.61048	0.8444444	0.2279495	0.10473684		
	4	8.68E-07	5.28E-06	1.19E-05	0.11114	0.36923	0.5288889	0.1643939	0.07294117		
at Bragg condition	1	2.27E-05	1.30E-05	2.28E-05	1	1	1	1.7461538	0.99561403		
	2	2.08E-05	1.40E-05	3.29E-05	0.9163	1.07692	1.4429825	1.4857142	0.63221884		
	3	8.96E-06	8.97E-06	2.31E-05	0.39471	0.69	1.0131579	0.998851	0.38787878		
	4	3.96E-06	5.47E-06	1.46E-05	0.17445	0.42076	0.6403509	0.7239488	0.27123287		
0.5 deg off Bragg condition	1	1.63E-05	1.43E-05	2.25E-05	1	1	1	1.1398601	0.72444444		
	2	1.67E-05	1.39E-05	2.79E-05	1.02454	0.97202	1.24	1.2014388			
	3	7.15E-06	8.73E-06	1.90E-05	0.43865	0.61048	0.8444444	0.8190148	0.37631578		
	4	2.86E-06	5.28E-06	1.19E-05	0.17546	0.36923	0.5288889	0.5416666	0.24033613		

0.45 DEG. MOSAIC SPREAD DATA (CONT.)											
		DATA	THEORY	THEORY	DATA	THEORY	THEORY	THEORY	DATA	DATA	
ANGLE	PEAK #	photons/electron	w/ scattering	w/o scattering	N(n)/N(1)	w/ Scattering	w/o scattering	N(n)/N(1)	VS. THEORY	VS. THEORY	
1.0 deg	1	9.12E-06	1.64E-05	2.27E-05	1	1	1	1	0.55609756	0.401762115	
off Bragg	2	6.57E-06	1.41E-05	2.20E-05	0.72039	0.8597561	0.969163	0.969163	0.46595744	0.298636364	
condition	3	2.50E-06	8.63E-06	1.39E-05	0.27412	0.5262195	0.6123348	0.6123348	0.28968713	0.179856115	
	4	1.01E-06	5.19E-06	8.44E-06	0.11075	0.3164634	0.3718062	0.3718062	0.19460501	0.119668246	
1.5 deg	1	3.99E-06	1.31E-05	1.58E-05	1	1	1	1	0.30458015	0.252531646	
off Bragg	2	2.31E-06	9.91E-06	1.22E-05	0.57895	0.7564885	0.7721519	0.7721519	0.23309788	0.189344262	
condition	3	8.20E-07	5.88E-06	7.30E-06	0.20551	0.448855	0.4620253	0.4620253	0.13945578	0.112328767	
	4		3.51E-06	4.36E-06		0.2679389	0.2759494	0.2759494			
2.0 deg	1	2.85E-06	9.18E-06	1.02E-05	1	1	1	1	0.31045751	0.279411765	
off Bragg	2	1.25E-06	6.44E-06	7.22E-06	0.4386	0.7015251	0.7078431	0.7078431	0.19409937	0.173130194	
condition	3		3.77E-06	4.23E-06		0.4106754	0.4147059	0.4147059			
	4		2.24E-06	2.51E-06		0.2440087	0.2460784	0.2460784			
2.5 deg	1	1.56E-06	6.46E-06	6.91E-06	1	1	1	1	0.24148606	0.225759768	
off Bragg	2	5.02E-07	4.37E-06	4.69E-06	0.32179	0.6764706	0.6787265	0.6787265	0.11487414	0.107036247	
condition	3		2.54E-06	2.73E-06		0.3931889	0.3950796	0.3950796			
	4		1.51E-06	1.62E-06		0.2337461	0.2344428	0.2344428			
3.0 deg	1	1.18E-06	4.71E-06	4.94E-06	1	1	1	1	0.25053078	0.238866397	
off Bragg	2	3.58E-07	3.12E-06	3.23E-06	0.30339	0.6624204	0.6538462	0.6538462	0.11474359	0.110835913	
condition	3		1.81E-06	1.90E-06		0.3842887	0.3846154	0.3846154			
	4		1.07E-06	1.13E-06		0.2271762	0.2287449	0.2287449			

1.31 DEG. MOSAIC SPREAD DATA											
ANGLE	PEAK #	DATA photons/electron	THEORY w/ scattering	THEORY w/o scattering	DATA N(n)/N(1)	THEORY w/ Scattering N(n)/N(1)	THEORY w/o scattering N(n)/N(1)	DATA	VS.THEORY w/ scattering	DATA	VS.THEORY w/o scattering
neg 2.5 deg from Bragg condition	1	1.10E-06	4.18E-06	6.90E-06	1	1	1	0.26315789	0.15942029		
	2	6.27E-07	2.78E-06	4.68E-06	0.57	0.6650718	0.6782609	0.22553956	0.133974359		
	3		1.62E-06	2.72E-06		0.3875598	0.3942029				
	4		9.57E-07	1.61E-06		0.2289474	0.2333333				
neg 2.0 deg from Bragg condition	1	2.35E-06	4.90E-06	1.02E-05	1	1	1	0.47959183	0.230392157		
	2	1.29E-06	3.33E-06	7.19E-06	0.54894	0.6795918	0.704902	0.38738738	0.179415855		
	3	4.28E-07	1.94E-06	4.21E-06	0.18213	0.3959184	0.4127451	0.22061855	0.101662708		
	4		1.15E-06	2.50E-06		0.2346939	0.245098				
neg 1.5 deg from Bragg condition	1	4.49E-06	5.19E-06	1.57E-05	1	1	1	0.86512524	0.285987261		
	2	2.85E-06	3.61E-06	1.21E-05	0.63474	0.6955684	0.7707006	0.78947368	0.23553719		
	3	9.96E-07	2.11E-06	7.25E-06	0.22183	0.4065511	0.4617834	0.47203791	0.13737931		
	4		1.25E-06	4.32E-06		0.2408478	0.2751592				
neg 1.0 deg from Bragg condition	1	1.08E-05	4.40E-06	2.24E-05	1	1	1	2.45454545	0.482142857		
	2	6.93E-06	3.14E-06	2.16E-05	0.64167	0.7136364	0.9642857	2.20700636	0.320833333		
	3	2.96E-06	1.85E-06	1.36E-05	0.27407	0.4204545	0.6071429	1.6	0.217647059		
	4	1.17E-06	1.10E-06	8.26E-06	0.10833	0.25	0.36875	1.06363636	0.141646489		
neg 0.5 deg from Bragg condition	1	1.66E-05	2.66E-06	2.21E-05	1	1	1	6.24060150	0.751131222		
	2	1.15E-05	1.95E-06	2.70E-05	0.69277	0.7330827	1.2217195	5.89743589	0.425925926		
	3	4.78E-06	1.15E-06	1.83E-05	0.28795	0.4323308	0.8280543	4.15652173	0.261202186		
	4	2.07E-06	6.85E-07	1.14E-05	0.1247	0.2575188	0.5158371	3.02189781	0.181578947		
at Bragg condition	1	1.90E-05	1.72E-06	2.23E-05	1	1	1	11.0465116	0.852017937		
	2	1.45E-05	1.29E-06	3.17E-05	0.76316	0.75	1.4215247	11.2403100	0.457413249		
	3	6.11E-06	7.62E-07	2.21E-05	0.32158	0.4430233	0.9910314	8.01837270	0.276470588		
	4	2.95E-06	4.54E-07	1.39E-05	0.15526	0.2639535	0.62333184	6.49779735	0.212230216		



1.31 DEG. MOSAIC SPREAD DATA (CONT.)									
		DATA	THEORY	THEORY	DATA	THEORY	THEORY	DATA	
		photons/electron	w/ scattering	w/o scattering	N(n)/N(1)	N(n)/N(1)	w/ scattering	VS.THEORY	DATA
ANGLE	PEAK #						N(n)/N(1)	w/ scattering	VS.THEORY
0.5 deg off Bragg condition	1	1.30E-05	2.66E-06	2.21E-05	1	1	1	4.88721804	0.588235294
	2	9.82E-06	1.95E-06	2.70E-05	0.75538	0.7330827	1.22171946	5.03589743	0.363703704
	3	3.74E-06	1.15E-06	1.83E-05	0.28769	0.4323308	0.8280543	3.25217391	0.204371585
	4	1.59E-06	6.85E-07	1.14E-05	0.12231	0.2575188	0.5158371	2.32116788	0.139473684
1.0 deg off Bragg condition	1	8.34E-06	4.40E-06	2.24E-05	1	1	1	1.89545454	0.372321429
	2	5.78E-06	3.14E-06	2.16E-05	0.69305	0.7136364	0.96428571	1.84076433	0.267592593
	3	2.25E-06	1.85E-06	1.36E-05	0.26978	0.4204545	0.60714286	1.21621621	0.165441176
	4	8.40E-07	1.10E-06	8.26E-06	0.10072	0.25	0.36875	0.76363636	0.101694915
1.5 deg off Bragg condition	1	4.22E-06	5.19E-06	1.57E-05	1	1	1	0.81310211	0.268789809
	2	3.02E-06	3.61E-06	1.21E-05	0.71564	0.6955684	0.77070064	0.83656509	0.249586777
	3	1.03E-06	2.11E-06	7.25E-06	0.24408	0.4065511	0.46178344	0.48815165	0.142068966
	4	4.72E-07	1.25E-06	4.32E-06	0.11185	0.2408478	0.27515924	0.3776	0.109259259
2.0 deg off Bragg condition	1	1.83E-06	4.90E-06	1.02E-05	1	1	1	0.37346938	0.179411765
	2	1.50E-06	3.33E-06	7.19E-06	0.81967	0.6795918	0.70490196	0.45045045	0.208623088
	3	1.18E-07	1.94E-06	4.21E-06	0.06448	0.3959184	0.4127451	0.06082474	0.028028504
	4		1.15E-06	2.50E-06		0.2346939	0.24509804		
2.5 deg off Bragg condition	1	1.04E-06	4.18E-06	6.90E-06	1	1	1	0.24880382	0.150724638
	2	5.80E-07	2.78E-06	4.68E-06	0.55769	0.6650718	0.67826087	0.20863309	0.123931624
	3		1.62E-06	2.72E-06		0.3875598	0.3942029		
	4		9.57E-07	1.61E-06		0.2289474	0.23333333		

2.5 DEG. MOSAIC SPREAD DATA											
		DATA	THEORY	THEORY	DATA	THEORY	THEORY	THEORY	DATA	DATA	
ANGLE	PEAK #	photons/electron	w/ scattering	w/o scattering	N(n)/N(1)	N(n)/N(1)	N(n)/N(1)	w/o scattering	VS.THEORY	VS.THEORY	
neg 2.5 deg	1	3.85E-06	1.72E-06	6.91E-06	1	1	1	1	2.238372093	w/o scattering	0.557163531
from Bragg	2	1.79E-06	1.13E-06	4.69E-06	0.46494	0.6569767	0.6787265	0.6787265	1.584070796	0.381663113	
condition	3	4.17E-07	6.51E-07	2.73E-06	0.10831	0.3784884	0.3950796	0.3950796	0.640552995	0.152747253	
	4		3.61E-07	1.62E-06		0.2098837	0.2344428				
neg 2.0 deg	1	3.53E-06	2.10E-07	2.26E-05	1	1	1	1	16.80952381	0.15619469	
from Bragg	2	1.79E-06	1.41E-07	3.25E-05	0.50708	0.6714286	1.4380531	1.4380531	12.69503546	0.055076923	
condition	3	4.17E-07	8.18E-08	2.27E-05	0.11813	0.3895238	1.0044248	1.0044248	5.097799511	0.018370044	
	4		4.85E-08	1.43E-05		0.2309524	0.6327434				
neg 1.5 deg	1	7.31E-06	1.29E-06	1.57E-05	1	1	1	1	5.666666667	0.465605096	
from Bragg	2	4.89E-06	1.05E-06	1.22E-05	0.66895	0.8139535	0.7770701	0.7770701	4.657142857	0.400819672	
condition	3	2.05E-06	6.10E-07	7.28E-06	0.28044	0.4728682	0.4636943	0.4636943	3.360655738	0.281593407	
	4	8.54E-07	3.61E-07	4.35E-06	0.11683	0.279845	0.2770701	0.2770701	2.36565097	0.196321839	
neg 1.0 deg	1	1.12E-05	8.36E-07	2.26E-05	1	1	1	1	13.39712919	0.495575221	
from Bragg	2	6.87E-06	5.56E-07	2.19E-05	0.61339	0.6650718	0.9690265	0.9690265	12.35611511	0.31369863	
condition	3	2.14E-06	3.23E-07	1.38E-05	0.19107	0.3863636	0.6106195	0.6106195	6.625386997	0.155072464	
	4		1.91E-07	8.37E-06	0	0.2284689	0.370354				
neg 0.5 deg	1	9.79E-06	3.95E-07	2.24E-05	1	1	1	1	24.78481013	0.437053571	
from Bragg	2	6.74E-06	2.64E-07	2.79E-05	0.68846	0.6683544	1.2455357	1.2455357	25.53030303	0.241577061	
condition	3	2.69E-06	1.54E-07	1.87E-05	0.27477	0.3898734	0.8348214	0.8348214	17.46753247	0.143850267	
	4	1.23E-06	9.09E-08	1.17E-05	0.12564	0.2301266	0.5223214	0.5223214	13.53135314	0.105128205	
at Bragg	1	1.13E-05	2.10E-07	2.26E-05	1	1	1	1	53.80952381	0.5	
condition	2	8.42E-06	1.41E-07	3.25E-05	0.74513	0.6714286	1.4380531	1.4380531	59.71631206	0.259076923	
	3	4.09E-06	8.18E-08	2.27E-05	0.36195	0.3895238	1.0044248	1.0044248	50	0.180176211	
	4	1.19E-07	4.85E-08	1.43E-05	0.01053	0.2309524	0.6327434	0.6327434	2.453608247	0.008321678	

2.5 DEG. MOSAIC SPREAD DATA (CONT.)											
ANGLE	PEAK #	DATA photons/electron	THEORY w/ scattering	THEORY w/o scattering	DATA N(n)/N(1)	THEORY w/ Scattering N(n)/N(1)	THEORY w/o scattering N(n)/N(1)	DATA w/ scattering	DATA VS. THEORY w/ scattering	DATA VS. THEORY w/o scattering	
0.5 deg	1	8.80E-06	3.95E-07	2.24E-05	1	1	1	22.27848101	0.392857143		
off Bragg	2	6.75E-06	2.64E-07	2.79E-05	0.76705	0.6683544	1.2455357	25.56818182	0.241935484		
condition	3	2.64E-06	1.54E-07	1.87E-05	0.3	0.3898734	0.8348214	17.14285714	0.141176471		
	4	1.00E-06	9.09E-08	1.17E-05	0.11364	0.2301266	0.5223214	11.00110011	0.085470085		
1.0 deg	1	7.45E-06	8.36E-07	2.26E-05	1	1	1	8.911483254	0.329646018		
off Bragg	2	5.98E-06	5.56E-07	2.19E-05	0.80268	0.6650718	0.9690265	10.75539568	0.273059361		
condition	3	2.32E-06	3.23E-07	1.38E-05	0.31141	0.3863636	0.6106195	7.182662539	0.168115942		
	4	9.12E-07	1.91E-07	8.37E-06	0.12242	0.2284689	0.370354	4.77486911	0.108960573		
1.5 deg	1	5.14E-06	1.29E-06	1.57E-05	1	1	1	3.984496124	0.327388535		
off Bragg	2	3.81E-06	1.05E-06	1.22E-05	0.74125	0.8139535	0.7770701	3.628571429	0.312295082		
condition	3	1.67E-06	6.10E-07	7.28E-06	0.3249	0.4728682	0.4636943	2.737704918	0.229395604		
	4	5.01E-07	3.61E-07	4.35E-06	0.09747	0.279845	0.2770701	1.387811634	0.115172414		
2.0 deg	1	3.47E-06	2.10E-07	2.26E-05	1	1	1	16.52380952	0.153539823		
off Bragg	2	2.30E-06	1.41E-07	3.25E-05	0.66282	0.6714286	1.4380531	16.31205674	0.070769231		
condition	3	7.82E-07	8.18E-08	2.27E-05	0.22536	0.3895238	1.0044248	9.5599022	0.034449339		
	4		4.85E-08	1.43E-05		0.2309524	0.6327434				
2.5 deg	1	3.21E-06	1.72E-06	6.91E-06	1	1	1	1.86627907	0.464544139		
off Bragg	2	1.41E-06	1.13E-06	4.69E-06	0.43925	0.6569767	0.6787265	1.247787611	0.300639659		
condition	3		6.51E-07	2.73E-06		0.3784884	0.3950796				
	4		3.61E-07	1.62E-06		0.2098837	0.2344428				
3.0 deg	1	3.67E-06	1.70E-06	4.93E-06	1	1	1				
off Bragg	2	1.79E-06	1.11E-06	3.28E-06	0.48774	0.6529412	0.6653144				
condition	3	6.13E-07	6.39E-07	1.90E-06	0.16703	0.3758824	0.3853955				
	4		3.78E-07	1.12E-06		0.2223529	0.2271805				



## LIST OF REFERENCES

1. Rule, D.W., and others, "Production of X-Rays by the Interaction of Charged Particle Beams with Periodic Structures in Crystalline Materials," paper no. 25 presented at SPIE's International Symposium on Optical Science and Engineering Conf. no. 1552 Short Wavelength Sources, San Diego, California, 21-26 July 1991.
2. Baryshevsky, V.G., and others, "Experimental Observation of Parametric X-Rays from Ultrarelativistic Electrons," J. Physics K: Applied Physics, v.19, pp. 171-176, 1986.
3. Evertson, S., "Experimental Considerations of Higher Order Parametric X-Rays From Silicon Crystals of Varying Thicknesses," Masters Thesis, Naval Postgraduate School, Monterey, California, June 1992.
4. DiNova, K.L., "Enhanced Higher Order Parametric X-Radiation Production," Masters Thesis, Naval Postgraduate School, Monterey, California, December 1992.
5. Rule, D.W., and others, "The Effects of Mosaicity on Theoretical Parametric X-Ray Spectra," Tomsk.
6. Feranchuk, I.D. and Ivanshin, A.V., "Theoretical Investigation of the Parametric X-Ray Features," J. Physique, v. T46, no. 11, pp. 1981-1986, November 1985.
7. Fasanello, T.J., "Solid State X-Ray Detector Calibration Techniques and LINAC Beam Intensity Measurements," Masters Thesis, Naval Postgraduate School, Monterey, California, December 1992.
8. Canberra Instruction Manual, Si(Li) Detector System Series 7300, S/N 1191404, revised January 1991.
9. Experiments in Nuclear Science AN34 Laboratory Manual, 3rd ed., Revised, pp. 167-168, EG&G Ortec Incorporated, 1984.
10. The Nucleus, Inc., "Personal Computer Analyzer Series II," copyright 1992.
11. Mosaic Spread Measurements provided by Ralph Fiorito, Naval Surface Warfare Center, Silver Spring, Maryland, November 3, 1994.
12. Borland, "QuattroPro v 4.0," copyright 1992.
13. Jandel Scientific, "PeakFit v 3.0 Software," copyright 1991 AISN Software.
14. Microsoft, "Microsoft Excel v 5.0," copyright 1985-1993.

15. Applied Inventions Corporation, "Photcoef", copyright 1989-1993.
16. Perkins, S.T., Tables and Graphs of Electron-Interaction Cross Sections from 10 eV to 100 eV, Lawrence Livermore National Laboratory, 1991.
17. Perkins, S.T., Tables and Graphs of Atomic Subshell and Relaxation Data, Lawrence Livermore National Laboratory, 1991.
18. Private conversation between K.L. DiNova, Defense Nuclear Agency, Alexandria, Virginia, and the authors, November 21, 1994.
19. Taylor, J.R., An Introduction to Error Analysis, University Science Books, 1982.
20. MathSoft Inc., "MathCad v 5.0+", copyright 1991-1994.

## INITIAL DISTRIBUTION LIST

1. Defense Technical Information Center.....2  
     Cameron Station  
     Alexandria, Virginia 22304-6145
  
2. Library, Code 52.....2  
     Naval Postgraduate School  
     Monterey, California 93943-5101
  
3. Dr. W. B. Colson, Code Ph/Cw.....1  
     Department of Physics  
     Naval Postgraduate School  
     Monterey, California 93943-5002
  
4. Mr. D. Snyder, Code 61PH.....1  
     Department of Physics  
     Naval Postgraduate School  
     Monterey, California 93943-5002
  
5. Mr. H. Rietdyk, Code 61PH.....1  
     Department of Physics  
     Naval Postgraduate School  
     Monterey, California 93943-5002
  
6. Dr. X. K. Maruyama.....20  
     Office of Technology Assessment  
     International Security & Space Program  
     600 Pennsylvania Avenue  
     Washington, D. C. 20510-8025
  
7. LT W. M. Buckingham, USN.....1  
     Naval Submarine School  
     Code N222 SOAC 95030  
     Box 700  
     Groton, Connecticut 06349-5700
  
8. LT L. R. Ivey, USNR.....1  
     RTC Staff  
     Building 1127  
     Great Lakes, Illinois 60088-5300

9. LCDR K. L. DiNova, USN.....1  
Headquarters, Defense Nuclear Agency  
Attention: Shock Physics Weapons Effects  
Alexandria, Virginia 22310-3398
10. Dr. R. B. Fiorito, Code R36.....1  
Naval Surface Warfare Center  
10901 New Hampshire Avenue  
Silver Spring, Maryland 20903-5000
11. Dr. D. W. Rule, Code R36.....1  
Naval Surface Warfare Center  
10901 New Hampshire Avenue  
Silver Spring, Maryland 20903-5000
12. Dr. M. A. Piestrup.....1  
2181 Park Boulevard  
Palo Alto, California 94306